Rapid reconfiguration of the functional connectome after chemogenetic locus coeruleus activation

Rapid Reconfiguration of the Functional Connectome after Chemogenetic Locus Coeruleus Activation

Valerio Zerbi[1,7]*#, Amalia Floriou-Servou[2,7#], Marija Markicevic[1,7], Yannick Vermeiren[3,5], Oliver Sturman[2,7], Mattia Privitera[2,7], Lukas von Ziegler[2,7], Kim David Ferrari[4,7], Bruno Weber[4,7], Peter Paul De Deyn[3,5,6], Nicole Wenderoth[1,7*], Johannes Bohacek[2,7*]

[1] Neural Control of Movement Lab, Department of Health Sciences and Technology, ETH Zürich, Switzerland

[2] Laboratory of Molecular and Behavioral Neuroscience, Institute for Neuroscience, Department of Health Sciences and Technology, ETH Zurich, Switzerland

[3] Department of Biomedical Sciences, Laboratory of Neurochemistry and Behavior, Institute Born-Bunge, University of Antwerp, Wilrijk (Antwerp), Belgium

[4] Experimental Imaging and Neuroenergetics, Institute of Pharmacology and Toxicology, University of Zurich, Switzerland

[5] Department of Neurology and Alzheimer Center, University of Groningen and University Medical Center Groningen (UMCG), Groningen, Netherlands

[6] Department of Neurology, Memory Clinic of Hospital Network Antwerp (ZNA) Middelheim and Hoge Beuken, Antwerp, Belgium

[7] Neuroscience Center Zurich, ETH Zurich and University of Zurich, Switzerland

 # equal contribution

*** corresponding authors:**

Valerio Zerbi: valerio.zerbi@hest.ethz.ch
Nicole Wenderoth: nicole.wenderoth@hest.ethz.ch
Johannes Bohacek johannes.bohacek@hest.ethz.ch

Lead Contact: Johannes Bohacek johannes.bohacek@hest.ethz.ch

All authors have read and approved the final version of the manuscript.

Summary

The locus coeruleus (LC) supplies norepinephrine (NE) to the entire forebrain and regulates many fundamental brain functions. Studies in humans have suggested that strong LC activation might shift network connectivity to favor salience processing. To causally test this hypothesis, we use a mouse model to study the impact of LC stimulation on large-scale functional connectivity by combining chemogenetic activation of the LC with resting-state fMRI, an approach we term "chemo-connectomics". We show that LC activation rapidly interrupts ongoing behavior and strongly increases brain-wide connectivity, with the most profound effects in the salience and amygdala networks. Functional connectivity changes strongly correlate with transcript levels of *alpha*-1 and *beta*-1 adrenoceptors across the brain, and functional network connectivity correlates with NE turnover within select brain regions. We propose that these changes in large-scale network connectivity are critical for optimizing neural processing in the context of increased vigilance and threat detection.

Highlights

- Chemo-connectomics combines chemogenetics (DREADDs) with resting-state fMRI
- Locus coeruleus (LC) activation rapidly increases brain-wide functional connectivity
- Connectivity changes correlate positively with adrenoceptor distribution
- LC activation shifts large-scale network connectivity towards salience processing

eTOC Blurb

Selective activation of the locus coeruleus (LC), which provides norepinephrine to the brain, induces anxiety. It also rapidly shifts brain-wide connectivity towards networks linked to salience, alertness and fear processing. This is most likely mediated by the spatially specific distribution of adrenoreceptors across the brain.

INTRODUCTION

The locus coeruleus (LC) is a small structure in the brainstem (with approximately 1500 neurons in each hemisphere in mice and 20'000 in humans) (Manaye et al., 1995; Sara and Bouret, 2012), which sends widespread efferent projections to almost the entire brain, and constitutes the major source of norepinephrine (NE) to most forebrain regions. Dysregulation of the LC-NE system has been implicated in numerous psychiatric pathologies including depression, anxiety, attention-deficit-hyperactivity disorder, post-traumatic stress disorder and neurodegenerative diseases (Bangasser et al., 2019; Fortress et al., 2015; Isingrini et al., 2016; McCall et al., 2015; Naegeli et al., 2018; Weinshenker, 2018). The ability to selectively change activity within the LC-NE system with optogenetic and chemogenetic manipulations has confirmed that the LC has a strong modulatory effect on various functional circuits related to wakefulness (Carter et al., 2010), cognitive performance and memory (Uematsu et al., 2017; Usher et al., 1999), and on stress-related behavioral responses including fear, anxiety and avoidance (Hirschberg et al., 2017; McCall et al., 2015, 2017). These widespread functional effects are in line with theories that the LC optimizes cognitive processes relevant for task performance or adaptive behaviors by rearranging neural activity within and between large-scale neuronal systems (Aston-Jones and Cohen, 2005; Bullmore and Sporns, 2009; van den Heuvel and Hulshoff Pol, 2010; Seeley et al., 2007).

Phasic LC activation, as triggered by salient stimuli, enhances cognitive performance and facilitates faster orienting towards (and processing of) task-relevant cues (Aston-Jones and Cohen, 2005; Berridge and Waterhouse, 2003; Sara and Bouret, 2012). In contrast, high tonic LC activity, as reliably and robustly triggered by various stressors, causes the release of substantial quantities of NE throughout the brain (Arnsten, 2009; Valentino and Van Bockstaele, 2008), which is thought to have a "circuit breaker" function that allows the interruption of ongoing neural activity and rapid reconfiguration of functional communication between brain regions (i.e. functional networks) (Arnsten, 2009; Corbetta et al., 2008). This rapid response is highly evolutionarily conserved, as it benefits survival by enhancing vigilance and enabling the selection of adaptive behaviors in threatening situations (Roeder, 2005). However, it has not been demonstrated directly that increased LC activity reconfigures functional neural networks across the brain, and it remains unknown how the widespread LC projections might achieve specificity for regulating specific networks. Some evidence suggests that strong LC activation by environmental cues, as observed during acutely stressful situations, plays an important role in activating networks that favor salience processing and action selection (Aston-Jones and Cohen, 2005; Hermans et al., 2014), and that regional specificity is achieved through the distribution of adrenergic receptors (Arnsten, 2009). In humans, acute stress exposure dynamically shifts large-scale network activity towards higher activation of the salience network, including the amygdala (van Marle et al., 2010), which is mediated by *beta*-adrenergic receptors (Hermans et al., 2011) and is thought to promote hypervigilance and threat detection at the cost of executive control (Corbetta et al., 2008; Hermans et al., 2014). However, direct involvement of the LC has not been proven, since it is impossible to selectively manipulate LC activity in humans.

To explore whether LC activation changes local and global network organization, we used a translational mouse model and applied a novel ‘chemo-connectomics’ approach, which combines (i) cell-specific chemogenetic manipulation of neural activity afforded by Designer Receptors Exclusively Activated by Designer Drugs (DREADDs) (Armbruster et al., 2007); with (ii) a brain-wide functional connectome analysis as revealed by resting state functional magnetic resonance imaging (rs-fMRI) in mice. This approach leverages the molecular tools and genome-wide resources available in mice and allows us to link functional connectivity with micro- and mesoscopic properties of the mouse brain. We asked (1) whether a selective increase of LC activity would change the functional connectivity profiling of large-scale brain networks or “connectome”, (2) if such network-wide effects are related to the known distribution of adrenergic receptor subtypes across the brain, and (3) whether changes in functional connectivity correspond to the levels of NE release in the target structures.

RESULTS

To selectively target the LC, we used transgenic mice that express codon-improved Cre-recombinase (iCre) under the dopamine-*beta*-hydroxylase (DBH) promoter (DBH-iCre mice, **Figure 1A**)(Parlato et al., 2007). We stereotactically delivered floxed excitatory DREADDs(Roth, 2016) (AAV5-hSyn-DIO-hM3Dq-mCherry; *hM3Dq-mCh*) or a control virus (AAV5-hSyn-DIO-mCherry; *mCh*) to the LC, thus restricting virus expression to DBH-positive noradrenergic neurons of the LC (**Figure 1B**). We assessed successful LC activation using pupillometry (Liu et al., 2017; Murphy et al., 2014; Reimer et al., 2016). After two minutes of baseline recording under light isoflurane anesthesia, we activated LC neurons by administering the potent DREADD activator clozapine at an ultra-low dose (0.03 mg/kg, i.p., **Figure 1C**) (Gomez et al., 2017). Within a minute of clozapine injection, we observed a strong increase in pupil diameter in the hM3Dq-mCh group, while pupil diameter of mCh mice did not change in response to clozapine injection and remained stable throughout the 10-minute recording session (**Figure 1D-F**). To show that our LC activation protocol is behaviorally relevant, we subjected mice to an open field test (OFT) immediately after clozapine injection and recorded their behavior for 30 minutes. In comparison to mCh mice, clozapine injection had profound effects on the behavior of hM3Dq-mCh mice. Several minutes after clozapine administration, hM3Dq-mCh mice showed strongly suppressed locomotor activity (**Figure 1G, H**), spent less time in the (more aversive) center of the open field (**Figure 1I, J**), performed less activity-related supported rears (**Figure 1K, L**) and less exploratory unsupported rears (**Figure 1M, N**)(Sturman et al., 2018). This is in line with previous findings that LC activation suppresses motor activity (Carter et al., 2010; Hirschberg et al., 2017) and increases anxiety (Hirschberg et al., 2017; Li et al., 2018; McCall et al., 2015). Because the LC is a highly sexually dimorphic structure, we assessed whether these findings hold true in female mice as well. We confirmed that after clozapine administration, hM3Dq-mCh females also showed reduced locomotor activity in the OFT (**Figure S1B, C**), spent less time in the center (**Figure S1D, E**), and performed fewer supported (**Figure S1F, G**) and unsupported rears (**Figure S1H, I**). To better characterize the effects of LC activation on behavior, we also tested these females in the light-dark box (LDB) for 30 minutes, immediately after clozapine injection (**Figure S1A**). Compared to mCh, hM3Dq-mCh mice spent much less time in the aversive light compartment of the box (**Figure S1J, K**), and more time in the dark compartment (**Figure S1L, M**). They also travelled less distance (**Figure S1N, O**), shuttled fewer times between the light and the dark compartment (**Figure S1P**), and performed fewer rears (**Figure S1Q, R**). These results indicate reduced exploratory behavior and increased anxiety. As the strong suppression of locomotor activity could also be due to locomotor impairment, we trained the same mice on the rotarod (Day 1), and then tested them on two consecutive days, without clozapine (Day 2) or with clozapine (Day 3, see **Figure S1A**). Both during training and testing, hM3Dq-mCh mice performed similarly before and after clozapine injection (**Figure S1S**), with no significant difference between groups or across daily trials (**Figure S1T, S1U**). Thus, the strong suppression in locomotor activity after LC activation is likely due to an increase in anxiety and not due to any gross locomotor impairment.

Next, we validated activation of LC neurons molecularly. To this end, we returned to the same male mice that were used for OFT testing and injected them again with clozapine, collected their brains 90 minutes later and assessed the neural activity marker cFos in the LC using immunohistochemistry. As expected, we observed a strong increase in cFos expression restricted to tyrosine hydroxylase-positive (TH+) noradrenergic neurons of the LC in hM3Dq-mCh mice, whereas cFos was virtually absent in mCh mice (**Figure 1O, P**). Because behavior testing and cFos staining were performed in the same mice, we correlated the locomotor activity of hM3Dq-mCh mice with the number of cFos-positive neurons in the LC. We found a strong negative correlation (**Figure 1Q**), showing that the strength of LC activation predicts the suppression in locomotion/exploration. Thus, our chemogenetic strategy specifically activates LC neurons and rapidly induces behavioral changes that last at least 30 minutes.

LC activation drives rapid increases in functional connectivity

We hypothesized that an increase of LC-NE activity would rapidly reconfigure large-scale brain networks as reflected by the functional *connectome*. We therefore acquired resting state-fMRI (rs-fMRI) data before and after hM3Dq-induced LC activation in a continuous imaging session. We kept mice under light isoflurane anesthesia (see methods) and recorded 15 min of baseline fMRI, before activating hM3Dq with clozapine (0.03 mg/kg, i.v.) (Markicevic et al., 2018). After the clozapine injection, we continued the fMRI recordings for 8 minutes (i.e. transitory period) followed by another 15 minutes where LC is expected to be robustly activated (i.e. active period), leading to a total uninterrupted scan time of 38 minutes (**Figure 2A**). Although a sustained increase in neural activity can be shown for at least two hours after hM3Dq-DREADD activation (Gomez et al., 2017), we limited the duration of the functional imaging session to reduce the accumulation of isoflurane over time, which might otherwise impact the local excitation-inhibition balance and neurovascular coupling (Aksenov et al., 2015).

We first tested whether the observed changes in whole-brain connectivity were time-locked to DREADD activation in hM3Dq-mCh mice, but not mCh mice. Functional connectivity (FC), defined as the Pearson's correlation of BOLD activity between two regions (for details see methods), was measured between 165 brain regions (nodes) using the Allen's Common Coordinate Framework over 38 non-overlapping time bins of 1 minute each. For each time bin, FC is measured between each pair of regions (edges), normalized to the subject's baseline connectivity (i.e. averaged across the first 15 minutes), and effect size is calculated using the standardized difference between the group means (Cohen's D, hM3Dq-mCh vs mCh). During the first 15 minutes (baseline) Cohen's D varied on average between -0.12 and +0.10 (average: -0.00, null-to-small effect), and did not demonstrate an appreciable spatial or temporal pattern. However, immediately after clozapine injection, the effect size rapidly and significantly increased for the remainder of the scan session, showing increased connectivity in hM3Dq mice relative to mCh controls **(Figure 2B, C)**. Effect sizes range on average from +0.21 to +0.38 (moderate effect) and up to +3.2 for individual edges (very strong effect). These findings show that changes observed in the connectome are temporally linked to the activation of the LC-NE system and occur within minutes after intravenous injection of clozapine in mice expressing hM3Dq.

Increased functional connectivity is dependent on LC-NE signaling

We next tested whether the DREADD-induced connectivity changes could be pharmacologically blocked by medetomidine, a selective agonist of the inhibitory adrenergic *alpha*-2 receptor. Through *alpha-2* autoreceptors, medetomidine suppresses LC firing and NE release (Jorm and Stamford, 1993; Lakhlani et al., 1997). After pre-treating mice with a bolus injection of medetomidine (0.05 mg/kg, i.v.), medetomidine was also continuously infused at 0.1 mg/kg/h i.v. to maintain its levels stable throughout the ensuing rs-fMRI session, as previously described (Grandjean et al., 2014). After 15 minutes of baseline recording, clozapine was again administered as described above (**Figure 2A**). Across all edges, Cohen's D did not vary significantly over-time, showing that medetomidine prevented DREADD-induced LC activation (**Figure 2D, E).**

To examine the effect of different anesthesia regimes on FC over-time, we compared the effect size in mCh mice between both anesthesia conditions (i.e. 1% isoflurane vs. 0.5% isoflurane+medetomidine). We found no significant differences between the two experimental conditions in the baseline and transient periods (**Figure S2**). However, Cohen's D was slightly increased in the active period, suggesting a reduction of connectivity across all edges in the isoflurane group. This is a well-known effect, most likely caused by the accumulation of isoflurane over-time (Bukhari et al., 2018). The net effect was, however, null-to-small (average: +0.04, min: -0.04, max: +0.129) and about 7 times smaller than the DREADD-driven effect. Collectively, our findings indicate that the substantial changes in connectivity after DREADD activation causally depend on activation of the LC-NE system, as they are induced by LC-specific stimulation, and blocked by an *alpha*-2 adrenergic agonist.

Spatial reconfiguration of the functional connectome after LC activation reflects transcript levels of adrenoceptors

Next, we mapped the location of the connections that were altered following LC activation. To this end, we compared the connectome matrix obtained from the first 15 minutes of the scan (baseline period) to the last 15 minutes of the scan (post clozapine, '*active* period'). The analysis of the functional connectome after LC-NE activation revealed a large group of edges that display increased FC in the hM3Dq-mCh animals compared to mCh after clozapine injection (218 edges, time × group interaction, non-parametric, randomized permutation testing, family-wise error (FWE) corrected with Network Based Statistics at $p<0.05$) (**Figure 3A**). The spatial distribution of these hyper-connected edges is widespread and involves 64% of the 165 brain regions considered in the analysis (105 ROIs) (**Figure 3B**), which is in line with the widespread afferent fibers originating from the LC (Aston-Jones, 2004; Schwarz and Luo, 2015).

The analyses presented above suggest that different brain areas show distinctive connectivity changes upon LC-NE stimulation. To investigate this hypothesis, we determined how LC activation changes the overall connectivity strength of a single brain area as quantified by the 'node modulation index' (NMI). The NMI is a surrogate marker which is obtained by averaging the effect size of connectivity changes induced by LC-NE stimulation across the top-10% connections of the brain area of interest (based on FC strength at baseline **Figure 3C;** see **Figure S3A-C** for a more detailed evaluation of other sparsity levels). This index has been used previously for quantifying connectivity alterations in psychiatric disorders (Yang et al., 2016), or pharmacologically-induced changes in connectivity (Preller et al., 2018).

As expected, the NMI varied across brain areas (**Figure 3D, E,** full list in **Table S1**). The strongest variations occurred in regions that are densely innervated by the LC, such as the primary sensory and somatomotor areas (Bouret and Sara, 2002), the claustrum (Crick and Koch, 2005), the prefrontal cortex (notably the agranular insular cortex; pre- and infralimbic cortices; the frontal pole; and anterior cingulate areas) (Arnsten, 2009; Hirschberg et al., 2017), several nuclei of the amygdala (McCall et al., 2017), the thalamus (Beas et al., 2018), and the association cortex (Arnsten, 2009) (**Figure 3D, E**).

The LC is a bilateral structure, and each locus primarily projects ipsilateral. Thus, we tested whether our LC stimulation would similarly affect the spatial patterns of FC within the left and the right hemispheres. We found remarkably similar changes in FC (**Figure S3D-F**) on each side. The distribution of the effect size for all edges is right-skewed in both left and right hemispheres (**Figure S3D, E**), demonstrating increased connectivity after LC activation. Further, the changes in each node expressed with the NMI were highly linearly correlated between left and right hemisphere (Pearson's correlation = 0.7764, $p<0.0001$, **Figure S3F)**.

We then took advantage of the unique availability of molecular data in the same mouse strain, and asked if the anatomical heterogeneity found in the connectivity-based NMI maps relates to the spatial distribution of adrenergic neurotransmitter receptors in the mouse brain. Gene transcript maps of adrenoceptors *alpha*-1 (subunits a-d), *alpha*-2 (subunits a-c), *beta*-1 and *beta*-2 were obtained from the Allen Mouse Brain Atlas (Lein et al., 2007). The similarity with NMI maps was quantified using the Spearman rank correlation coefficient (*Rho*) across all 165 brain areas of the Allen's Common Coordinate Framework. After correcting for testing multiple independent hypotheses, we found that the transcriptional maps of all adrenoceptors display a significant correlation with the NMI, with the exception of *beta*-2 adrenergic receptors (**Figure 4A-D**). All these correlations display a higher than chance Spearman's rho value ($p<0.0001$ against a null distribution generated using 100.000 random permutations). We additionally compared our MNI maps against all dopamine (D1, D2, D3, D4, D5), serotonin (Htr1, Htr2, Htr3, Htr4, Htr5, Htr6, Htr7) and cholinergic (muscarinic 1, 2, 3, 4, 5 and nicotinic *alpha*-1, 4, 6, 7, *beta*-1, 2, delta, epsilon, gamma) receptors, to assess the specificity of our results (**Figure S4**). We found a significant Spearman's correlation with both D1 ($Rho=0.4014$, $p_{FDR}=9.11e^{-7}$)

and D4 (*Rho*=0.3789, $p_{FDR}=3.12e^{-6}$) receptors, which survived permutation testing and FDR correction (**Figure S4B, C**), but not with D2, D3 and D5 (**Figure S4A**). We also found significant correlations with cholinergic nicotinic *alpha*-1 (*Rho*=0.3302, $p_{FDR}=6.38e^{-5}$) and gamma subunits (*Rho*=0.3887, $p_{FDR}=1.85e^{-6}$) (**Figure S4D, E**), while none of the cholinergic muscarinic receptors or serotonin receptors exhibited correlations above chance level (**Figure S4A**). To account for spatial co-expression of different receptor types, we performed control analyses where dopaminergic, cholinergic or adrenergic receptors were added as co-variates into different partial correlation analysis models (see **Table S2** for details). We still found strong correlations between NMI and the spatial distribution of adrenergic *beta*-1 (*Rho*=0.2623, $p_{FDR} = 7.75e^{-4}$) and *alpha*-1 (*Rho*=0.2519, $p= 4.11e^{-3}$) receptors, and moderate correlations between NMI and dopamine receptors D1 (*Rho*=0.2005, $p_{FDR} = 0.0179$) and D4 (*Rho*=0.2219, $p_{FDR} = 0.0063$). By contrast, none of the correlations between NMI and the nicotinic cholinergic receptor distributions remained significant, once we entered adrenergic receptor distributions as co-variates into the model. This analysis suggests that the correlation between nicotinic cholinergic receptors and NMI might have been driven by the spatial co-expression of adrenergic *beta*-1 and *alpha*-1 receptors. Overall, these results represent the first brain-wide FC mapping in response to LC activation, revealing an anatomically specific *connectomic fingerprint* of LC hyperactivity, which maps well onto the spatial distribution of specific adrenoceptors and dopamine receptors.

LC increased connectivity within large-scale resting-state networks

Thus far, our data driven analyses focused on changes in connectivity between anatomically-defined pairs of brain regions. However, it is well known that there are sets of brain areas, so-called resting-state networks (RSNs), which exhibit synchronous neural activity and can be consistently identified in the mammalian brain. Connectivity-strength within a network can be quantified as the relative synchronization of BOLD activity across all voxels forming a RSN, and this measurement has been linked to local electrophysiological properties, behavioral performance, and severity of neurological disease (Rosazza and Minati, 2011). Here, we examined whether LC activation influences synchronization within large-scale RSNs, by calculating the spatial extent and connectivity strength for thirteen maximally-independent RSNs of the mouse brain. The topography of the RSNs was obtained from an independent cohort of wild-type mice (for a complete list and spatial distribution of the networks obtained with independent component analysis please refer to (Zerbi et al., 2015)). Overall effects within each RSN are determined by measuring a connectivity-strength index (using a Linear Mixed-Model, see (Zerbi et al., 2018)). Moreover, we investigated which voxels within each RSN significantly changed their level of synchronization upon LC-NE stimulation (using a dual regression approach).

In 6 out of 13 RSNs, we found significant group x time interactions resulting from an increase of within-network connectivity in the hM3Dq-mCh group, which was in stark contrast to the slight decrease in connectivity observed in the mCh group (**Figure 5**). The latter effect is likely attributable to an accumulation of isoflurane over time (Bukhari et al., 2018) (see **Figure S2**) which is, however, clearly reversed upon LC activation. We observe the strongest differences in two networks previously linked to LC activity in humans exposed to stress (Hermans et al., 2014): (1) the Salience Network (hyperconnectivity in agranular insular area, anterior cingulate, ventro-medial striatum, accumbens, globus pallidus, parafascicular nucleus of the thalamus and hippocampus; **Figure 5A**), and (2) the Amygdala Network (hyperconnectivity in basomedial and basolateral amygdala, claustrum, sub-thalamic nucleus and zona incerta; **Figure 5B**). Additionally, LC activation also increased connectivity within the Association/Auditory Network (**Figure 5C**), the Dorsal Hippocampus Network (**Figure 5D**), the Striato-Motor Network (**Figure 5E**), and the Antero-Posterior Retrosplenial/Default-Mode-Network (**Figure 5F**). These results suggest that LC activation expands the synchrony of signals in several large-scale networks, most significantly in the Salience and Amygdala Networks. These results are remarkably similar to those in humans, showing that acute stress increases FC within homologous salience/amygdala

networks (Hermans et al., 2011; van Marle et al., 2010) in a *beta*-adrenergic receptor-dependent manner (Hermans et al., 2011).

Network connectivity changes correlate with norepinephrine and dopamine turnover

After completion of the two rs-fMRI sessions, mice were given one/two weeks to recover (see methods). Eight hM3Dq-mCh mice and five mCh controls were injected again with clozapine (0.03 mg/kg, i.p.), and their brains were collected 90 minutes later to address two important issues; first, we wanted to ensure that clozapine exclusively activated noradrenergic LC neurons, and that activation occurred in all hM3Dq-mCh mice but not in the mCh controls. Second, we wanted to assess whether LC activation led to measurable NE release in target regions throughout the brain, and whether NE levels would correlate with observed changes in network connectivity. In order to address these two issues in each individual mouse, we pursued a two-pronged strategy for tissue processing (**Figure 6A**): Freshly collected brains were split with a razorblade along the superior colliculus to collect one section containing the LC for immunohistochemistry, and a second section containing the forebrain. From the forebrain section, we rapidly dissected cerebral cortex, hippocampus and dorsal striatum on ice. Samples were snap frozen and processed for analysis of monoamines and their metabolites using reversed-phase ultra-high-performance liquid chromatography (uHPLC) coupled with electrochemical detection (**Figure 6A**).

Co-labelling for TH and cFos revealed that clozapine injection only induced a strong and reliable activation of noradrenergic neurons in the LC of the hM3Dq-mCh mice (representative image in **Figure 6B**, sections of all mice presented in **Figure S5**). This validates that LC activation was successful in the mice undergoing fMRI scans. In parallel, we used uHPLC to measure and quantify the monoaminergic neurotransmitters norepinephrine (NE), dopamine (DA) and serotonin (5HT), as well as their main metabolites 3-methoxy-4-hydroxyphenylglycol (MHPG, metabolite of NE), homovanillic acid (HVA, metabolite of DA), 3,4-dihydroxyphenylacetic acid (DOPAC, metabolite of DA), and 5-hydroxyindoleacetic acid (5-HIAA, metabolite of 5HT). Because the measurement in whole tissue does not per se differentiate between intra- and extracellular neurotransmitter levels, this approach is mainly targeted towards measuring neurotransmitter ratios of (main) end stage metabolite over monoamine (e.g. MHPG/NE ratio) as an index of neurotransmitter turnover (e.g. NE turnover) and thus neuronal activity. We were able to reliably detect and quantify all measured compounds (see representative chromatographs in **Figure S6A, B).** NE levels decreased in all brain regions (**Figure 6C**), suggesting that LC activation for 90 minutes had reduced NE storage vesicles, as would be expected after sustained high-frequency firing. In agreement, MHPG levels increased in all brain regions (**Figure 6D**), resulting in a very strong increase in catabolic NE turnover (MHPG/NE, **Figure 6E**), and thus indicating overall high demanding neuronal NEergic activity. Dopamine levels were not changed in any of the brain regions under investigation (**Figure 6F**), yet we observed a robust increase in both hippocampal HVA and DOPAC (**Figure 6G, H**), and a small but significant increase of HVA in the cortex (**Figure 6G**). Dopamine turnover ratios (HVA/DA and DOPAC/DA) were increased in the hippocampus but not in striatum or cortex (**Figure 6I, J**). These results are in line with recent evidence that LC neurons can release DA in certain brain regions including the hippocampus(Beas et al., 2018; Kempadoo et al., 2016; Smith and Greene, 2012; Takeuchi et al., 2016). Our data newly suggest that DA release from LC neurons may be biased towards the hippocampus compared to the cortex and striatum. Epinephrine, 5-HT and 5-HT turnover ratios were not altered in any of the brain regions sampled (**Figure S6C-F**).

As we performed fMRI and uHPLC analyses in the same mice (although with a temporal delay of 1 week and in response to separate injections with clozapine), we were able to conduct a correlation analysis between individual differences in neurotransmitter turnover and corresponding changes in network connectivity. We found positive correlations between the NE and DA turnover ratios in the cortex and changes in FC within the Salience Network (**Figure 6K, Figure S6G, J**), as well as between NE and DA turnover ratios in the hippocampus and FC in the Hippocampus Network (**Figure 6L,**

Figure S6H, K). NE turnover in the striatum, but not DA turnover, correlated with FC changes in the Striato-Motor Network (**Figure 6M, Figure S6I, L)**. Importantly, we observed no correlation between 5-HT levels/turnover and the respective network connectivity changes in any of the brain regions tested (**Figure S6M-O**). These results collectively suggest that brain network changes we observe with rs-fMRI are tied to the amount of NE and/or DA released in a given region.

LC neurons project sparsely to the dorsal striatum (caudate-putamen)

Although increased NE turnover in the cortex and hippocampus was expected due to strong innervation by the LC, the increased NE turnover in the dorsal striatum (consisting of caudate and putamen) (Models, 2005) was surprising, because this region is widely thought to be devoid of NE projections (Aston-Jones, 2004; Berridge and Waterhouse, 2003). In agreement with increased striatal NE turnover, we also observed a strong increase in the node modulation index (NMI) in the caudate-putamen (**Figure 3E**), and increased functional connectivity within the large-scale Striato-Motor Network (**Figure 5E**). Thus, we decided to first test whether we could detect noradrenergic axons within the caudate-putamen. We stained for the norepinephrine reuptake transporter Slc6a2 (NET), which is expressed exclusively in noradrenergic cells (Mulvey et al., 2018; Schroeter et al., 2000). Although the caudate-putamen appears devoid of NET compared to the intense NET staining seen in the adjacent cortex (**Figure 7A**), we clearly detected long, thin axons in the caudate-putamen (**Figure 7B**). To investigate whether these axons originate from LC neurons, we delivered a retrograde AAV2 virus (Tervo et al., 2016) carrying floxed mCherry into the dorsolateral caudate-putamen of DBH-iCre mice. Seven weeks after virus injection, we stained the LC and detected a clearly recognizable subset of LC neurons that expressed mCherry in transgenic animals (n=3) but not in a wild-type control animal (n=1) (representative images from each animal shown in **Figure 7C** and **Figure S7**). We were able to reproduce these findings with a second Cre-dependent retrograde AAV2 virus that expresses EGFP (**Figure 7D**), which also allowed us to detect axons in the caudate-putamen that were co-labelled with both EGFP and NET (**Figure 7E**). Together, these data show that there are sparse projections from LC to the caudate-putamen. These projections could account for the increase in NE levels detected in the striatum after LC stimulation, as well as for the increased functional connectivity observed in the caudate-putamen and in the large-scale Striato-Motor Network.

DISCUSSION

Revealing the connectomic fingerprint of norepinephrine release after LC activation

Neuromodulatory systems of the brain track and integrate environmental signals, exert powerful control over neuronal function, and are the primary targets of most neuropsychiatric treatment strategies (Avery and Krichmar, 2017; Berton and Nestler, 2006; Lee and Dan, 2012). Human neuroimaging data suggest that norepinephrinergic neuromodulation dynamically influences long-range neural communication, thereby strengthening specific functional networks to facilitate task performance (Shine et al., 2016, 2019). It is, however, challenging to study the impact of an individual neuromodulatory system across large-scale neuronal networks. The advent of optogenetics and chemogenetics, combined with advances in rodent imaging capabilities, now enables us to link circuit-level manipulations to global network changes. Recent studies have used these approaches to show that selective manipulation of dopamine (Lohani et al., 2017; Roelofs et al., 2017) and serotonin (Giorgi et al., 2017) release can lead to global activity changes measured by fMRI. Our work extends these studies by assessing the role of the LC-NE system in assembling and rearranging connectivity within and between well-defined large-scale neuronal systems using rs-fMRI. The chemo-connectomic approach establishes the framework necessary to link the activity of neuromodulatory systems to clinically relevant brain signals and their neuroanatomical substrates.

Adrenoceptor distribution as an organizing principle affording "global specificity"

Neurons in the LC are topographically organized based on their widespread efferent projections (Aston-Jones, 2004; Schwarz and Luo, 2015), and circuit-based approaches reveal functional specificity of sub-populations of LC neurons based on their target projection regions (Hirschberg et al., 2017; Uematsu et al., 2017). LC neurons appear to form neuronal ensembles, which can be activated in response to isolated sensory stimuli (Totah et al., 2018a, 2018b). With increasing stimulus strength, more LC-ensembles can be activated, leading to "global" LC activation in response to strong stimuli (such as stress exposure) (Totah et al., 2018b). Widespread NE release in response to this global LC activation is commonly thought to act as a broadcast signal, which modulates local electrophysiological properties, gearing specific networks towards integrating environmental information, allowing to select/trigger adequate behaviors (Schwarz and Luo, 2015; Usher et al., 1999). We hypothesized that the distribution of adrenoceptors enables network specific effects of "global" NE release. Indeed, we observed strong correlations between functional connectivity (FC) and expression levels of *alpha*-1 and *beta*-1 adrenoceptors, which were maintained over-and-above the effect explained by the distribution of other receptor types. This is in line with the finding that *alpha*-1 and *beta*-1 adrenoceptors have low binding affinity for NE and are thus only activated in response to high levels of NE release (Arnsten, 2009; Berridge and Waterhouse, 2003). We found weaker correlations with inhibitory adrenergic *alpha*-2 receptors, dopaminergic D1 and D4 receptors, and cholinergic nicotinic *alpha*-1 and *gamma* receptor subunits. However, multiple regression analyses indicate that correlations between FC and cholinergic nicotinic receptors and *alpha*-2 adrenoceptors may be driven by the spatial co-expression with *alpha*-1 and *beta*-1 adrenoceptors. *Alpha*-2 adrenoceptors are known to have a much lower affinity for NE, thus their signaling contribution is smaller during strong NE release that activates *alpha*-1 and *beta*-1 receptors (Arnsten, 2009). However, definitive conclusions regarding the contribution of individual receptors to the observed effects on connectivity would require local administration of specific receptor antagonists. The absence of a correlation with *beta*-2 adrenergic receptors was unexpected, given that both *beta*-1 and *beta*-2 adrenoceptors are ubiquitously expressed and have similar binding affinity for NE (Ramos and Arnsten, 2007). It is possible that *beta*-2 receptors indeed do not play a role in the NE-induced effects on network connectivity, as contrasting effects of *beta*-1 and *beta*-2 receptors on working memory performance have previously been reported(Ramos et al., 2005, 2008). However, it is also possible that technical limitations mask an involvement of *beta*-2 adrenoceptors, given that we attempt to align our connectivity data with publicly available spatial gene expression maps of individual receptor densities. Compared to previous work that has correlated connectivity measures of a brain area with the transcriptional profile across a large number of genes (Fulcher and Fornito, 2016; Rubinov et al., 2015), correlations with a single gene are more susceptible to noise in gene-expression data. Therefore, we believe that the strong correlations between NMI and beta-1/alpha-1 adrenoceptors are evidence for a robust relationship, while weak gene-NMI correlations should be interpreted with caution and cannot be used to infer the absence of an association.

LC activation recapitulates many of the complex effects triggered by stress exposure

Modern theories of LC function propose that LC activation serves to optimize the trade-off between exploitation and exploration, with strong, global LC activity causing interruption of ongoing activity to enable the selection of appropriate behaviors (Aston-Jones and Cohen, 2005). Global LC activity is robustly triggered by noxious/stressful stimuli (Berridge and Waterhouse, 2003; Valentino and Van Bockstaele, 2008), which induce anxiety and reduce exploratory activity, through circuits involving the amygdala and prefrontal cortex (Hirschberg et al., 2017; Li et al., 2018; McCall et al., 2015, 2017; Uematsu et al., 2017). Our DREADD-induced activation of the LC similarly reduces exploratory activity and increases anxiety, and globally induces cFos expression throughout the LC.

Therefore, our global LC activation likely resembles peak LC activity that would normally be triggered by stressful stimuli.

Our data are well in line with findings in humans where acute stress exposures (induced by aversive movies or social stressors) increased FC in the Salience Network (van Marle et al., 2010) and Default Mode Network (Vaisvaser et al., 2013). Similarly, acute stress leads to increased interconnectivity and positive BOLD responses within several cortical regions related to salience processing (frontoinsular, anterior cingulate, inferotemporal, and temporoparietal) and subcortical regions (amygdala, striatum, thalamus, hypothalamus, hippocampus and midbrain) as a function of stress response magnitude (Hermans et al., 2011; van Oort et al., 2017; Seo et al., 2011; Sinha et al., 2004). Notably, increased connectivity in the Salience Network was blocked by systemic administration of a *beta*-adrenergic receptor antagonist (propranolol) (Hermans et al., 2011). Given that LC activation is only one aspect of the highly complex changes observed during an acute stress response (Joëls and Baram, 2009), and considering that our analyses were performed in lightly anesthetized mice, it is remarkable that our results for the Salience Network, the Amygdala Network, and also the Default-Mode Network closely resemble fMRI and rs-fMRI findings described after acute stress exposures in humans(Hermans et al., 2014; van Oort et al., 2017) (**Figure 5**). Since our model allowed us to selectively and directly manipulate LC activity with DREADDs, our results causally show that selective LC activation rapidly reorganizes functional connectivity within specific large-scale networks. The rapid onset of the connectomic effects within minutes after LC activation points towards a direct, causal effect mediated by NE release throughout the forebrain.

Long-lasting hyperactivity of the LC is often observed after severe or chronic stress exposures (Borodovitsyna et al., 2018; Mana and Grace, 1997) and is considered a hallmark feature of post-traumatic stress disorder (PTSD) (Naegeli et al., 2018; Pietrzak et al., 2013). Two recent rs-fMRI studies showed - in both rats and mice - that chronic stress exposure resulted in large-range increases in functional network connectivity for regions including prelimbic/infralimbic areas, amygdala, cingulate cortex and hippocampus (Grandjean et al., 2016; Magalhães et al., 2018). In PTSD patients, fMRI reveals network wide changes in the amygdala, insula, hippocampus and anterior cingulate cortex (Fitzgerald et al.; Liberzon and Phan, 2003). Therefore, the changes observed after chronic stress exposure in rodents and in PTSD patients are strikingly similar to the effects of selective LC stimulation. Hyperactivity of the LC represents only one aspect of the multifaceted changes occurring in stress-related pathologies, but our data provide additional evidence that modulating LC activity might be a promising therapeutic approach (Bangasser and Valentino, 2014; Borodovitsyna et al., 2018).

One limitation of our approach is that fMRI requires anesthesia, thus we cannot assess how selective LC manipulations would modulate network activity/connectivity during task performance. An important role for the NE system is to modulate ongoing neural activity, and to control neuronal gain (signal-to-noise ratio) (Mather et al., 2016; Sara and Bouret, 2012). Further, the effects of NE on brain function are task dependent, and recent work on memory consolidation shows that noradrenergic activity in the amygdala itself influences large-scale networks (Barsegyan et al., 2019). Therefore, the role of NE on brain-region specific activity during task performance needs to be carefully assessed in future studies, when task-relevant networks are specifically engaged, while other networks will be actively suppressed.

Functional connectivity after LC activation involves dopamine release and dopamine receptors

Several recent reports have shown that dopamine (DA) can be co-released from LC terminals in the hippocampus (Kempadoo et al., 2016; Smith and Greene, 2012; Takeuchi et al., 2016) and thalamus (Beas et al., 2018). We also detect a strong increase in DA turnover in the hippocampus, and a subtle increase in the cortex (with no effects in the striatum). Our cortex samples contained heterogeneous regions, it is likely that specific cortical subregions (e.g. mPFC) display stronger changes in DA turnover. In concordance with our data, previous microdialysis experiments have detected release of

both DA and NE in the medial prefrontal cortex after chemical or electrical activation of the LC, while the same stimulations increased NE but not DA in the nucleus accumbens and caudate nucleus (Devoto et al., 2005b, 2005a; Kawahara et al., 2001). Together, our data provide new evidence for a regionally restricted role of DA release in response to LC stimulation. Future studies will have to test whether all LC neurons (or only selected sub-populations with specific projection targets) are able to release DA, and if specific interactions at the projection site are required to enable DA release. Finally, it remains unclear whether this co-release occurs under physiological conditions, as evidence suggests that it depends on the firing rate of individual LC neurons (Devoto et al., 2005b).

LC-induced synchronization in the dorsal striatum (caudate-putamen)

Although close interactions between dopaminergic and noradrenergic systems have long been recognized (Antelman and Caggiula, 1977), the dorsal striatum (caudate-putamen) is widely thought to be devoid of noradrenergic projections (Aston-Jones, 2004; Berridge and Waterhouse, 2003), and indeed staining for the NE transporter (NET, **Figure 7A**) or DBH (Swanson and Hartman, 1975) shows a strong depletion in the caudate-putamen. Given these data, we were surprised when our connectome analysis revealed that LC activation increased the strength of connectivity of the caudate-putamen (**Figure 3C**). Further, we observed synchronization of rs-fMRI activity in the Striato-Motor Network, which positively correlated with increased NE turnover in the same region (**Figure 6M**). Indeed, several studies have shown fairly high levels of NE (Schallert et al., 1978) in the caudate-putamen, as well as extracellular striatal NE increase after mild stress (handling) (Ihalainen et al., 1999) or LC stimulation (Devoto et al., 2005a). Adrenergic *alpha*-1, *alpha*-2 and *beta*-1 receptors are abundantly expressed on striatal pre- and post-synaptic membranes and cell bodies (Hara et al., 2010; Nicholas et al., 1996; Paschalis et al., 2009; Pisani et al., 2003; Rommelfanger et al., 2009), and *beta*-adrenergic receptor binding density is very high in the caudate-putamen of rodents and humans (Bylund and Snyder, 1976; Palacios and Kuhar, 1980; Reisine et al., 1979). Our results show that a considerable number of LC neurons directly project to the caudate-putamen, which is in line with early retrograde tracing work (Mason and Fibiger, 1979) but was rarely recognized in more recent literature. These findings may be relevant for Parkinson's disease, where an involvement of the LC-NE system is increasingly being recognized (Vermeiren and De Deyn, 2017; Weinshenker, 2018).

Conclusions

Using the novel chemo-connectomics approach presented here, we provide the first brain-wide analysis of connectome reconfiguration in response to selective LC activation. We show a profound, rapid and specific activation of large-scale networks related to salience processing, which occurs within minutes after clozapine administration specifically in mice expressing DREADDs. These effects are observed similarly in each hemisphere and they are blocked by activating presynaptic, auto-inhibitory *alpha*-2 adrenoceptors. Shifts in large-scale network connectivity correlate spatially with the distribution of adrenergic and dopaminergic receptor levels and with (post-mortem) measurements of NE, DA, and their metabolites in a within-subject design. These network effects are accompanied by increased pupil size and heightened anxiety, suggesting that the observed changes in brain network organization ultimately serve to promote vigilance and threat detection.

Acknowledgements

We thank Han-Yu Lin for genotyping and help with image analysis and all animal caretakers of the EPIC animal facility. We thank Jean-Charles Paterna from the Viral Vector Facility (VVF) of the Neuroscience Center Zurich, a joint competence center of ETH Zurich and University of Zurich for producing viral vectors and viral vector plasmids. We thank Prof. Isabelle Mansuy for generously

providing support and space in her lab. We thank Dr. Ben Fulcher for providing the gene-expression data and help with the correlational analyses, and Pierre-Luc Germain for feedback on statistical analyses. We thank Tilo Aurelio Gschwind for guidance on cFos immunohistochemistry, Ladina Hösli for helpful advice during the Rotarod experiments, and Prof. Markus Rudin for the use of the MRI facilities.

VZ is supported by ETH Career Seed Grant SEED-42 54 16-1 and by the SNSF AMBIZIONE PZ00P3_173984/1. AFS is supported by the Neuroscience Center Zurich (ZNZ) PhD Grant, the Swiss Foundation for Excellence and Talent in Biomedical Research, and the EMDO foundation. MM is supported by the Research Grant ETH-38 16-2. The lab of JB is funded by the ETH Zurich, SNSF Project Grant 310030_172889/1, the Forschungskredit of the University of Zurich (grant no. FK-15-035), the Vontobel-Foundation, the Novartis Foundation for Medical Biological Research, the Olga Mayenfisch Foundation and the Betty and David Koetser Foundation for Brain Research. Funding of uHPLC analyses was covered by Alzheimer Foundation Belgium (SAO-FRA) research grant (P#16003) and support of a Joint Programming Initiative Neurodegenerative Diseases (JPND) Multinational research project HEROES – ZonMw project N° 733051072.

Author Contributions

Conceptualization, VZ,AFS,NW,JB; Methodology, VZ, AFS, KDF,MM,OS,LvZ; Investigation, VZ,AFS,MM,YV,MP,OS; Writing – Original Draft, VZ,AFS,YV,NW,JB; Writing – Review & Editing, VZ,AFS,MM,YV,OS,MP,KDF,LvZ,BW,PPDD,NW,JB.; Funding Acquisition, VZ,AFS,BW,PPDD,NW,JB; Resources, BW,PPDD.; Supervision, VZ,NW,JB.

Declaration of Interests

The authors declare no competing interests.

Figure Legends

Figure 1. Physiological, behavioral and molecular effects of LC activation with hM3Dq. (**A**) Schematic of *DBH*-iCre mouse genetics. (**B**) mCherry (mCh) co-localizes with tyrosine hydroxylase (TH) in the LC of DBH-iCre mice after stereo-tactic delivery of AAV5-Syn1-DIO-mCh. (**C**) Diagram of the experimental design. (**D**) Images showing the pupil size before and after administration of clozapine in a mouse expressing hM3Dq-mCh in LC. (**E, F**) Pupil size increased after clozapine administration only in hM3Dq-mCh mice (interaction time x group: $F(1,10)=9.60$, $p=0.0113$, two-way ANOVA with Sidak *post hoc* tests). (**G-N**) Immediately after clozapine injection, hM3Dq-mCh mice travelled less distance than mCh control mice (**G, H:** main effect of group: $F(1,10)=21.92$, $p=0.0009$, two-way ANOVA), spent less time in the center (**I, J:** main effect of group $F(1,10)=5.15$, $p=0.0467$; interaction: $F(9,90)=3.04$, $p=0.0032$, two-way ANOVA with Sidak *post hoc* tests), per-formed fewer supported rears (**K, L:** main effect of group: $F(1,10)=7.24$, $p=0.0227$) and fewer unsupported rears (**M, N:** main effect of group: $F(1,10)=11.33$, $p=0.0072$, interaction: $F(9,90)=2.46$, $p=0.0148$). (**O**) Representative images of cFos expression in TH+ neurons in the LC of hM3Dq-mCh or mCh mice, 90 minutes after injection of clozapine. (**P**) Quantification of cFos expression showing increased neuronal activation in hM3Dq-mCh mice ($t(10)=5.12$, $p=0.0005$, unpaired t test). (**Q**) cFos expression in LC correlates with distance travelled in the OFT in hM3Dq-mCh mice ($r(5)=-0.8782$, $p=0.0093$). hM3Dq-mCh (n=7), mCh (n=5). *=$p<0.05$, **=$p<0.01$, ***=$p<0.001$. Data represent mean ± SEM. All scale bars: 50 μm. See also Figure S1.

Figure 2. DREADD activation of the LC causes time-locked changes in functional connectivity. (**A**) Schematic of the experimental set-up for MRI recordings. 4 weeks after bilateral virus delivery, mice underwent two MRI sessions with the same experimental procedure but different anesthetic regimes. Effect-size (Cohen's D) analysis of Functional Connectivity (FC) is shown for single-edges (n=2724) (**B**) and for the average across all edges (**C**). The data reveal time-locked increases in connectivity in multiple edges, starting immediately after clozapine (0.03 mg/kg) i.v. injection (Wilcoxon two-tailed test: $p=0.804$ for baseline period, $p=0.015$ for transient period and $p<0.0001$ for active period). (**D, E**) Treatment with the *alpha*-2 adrenergic agonist medetomidine (0.05 mg/kg + 0.1mg/kg/h, see methods) abolishes clozapine-induced effects between hM3Dq-mCh and mCh groups (Wilcoxon two-tailed test: $p=0.805$ for baseline period, $p=0.937$ for transient period, and $p=0.978$ for active period). *=$p<0.05$, ****=$p<0.0001$, NS=not significant. hM3Dq-mCh (n=11), mCh (n=7). See also Figure S2.

Figure 3. A whole-brain map showing the *connectome* after DREADD-induced LC activation. (**A**) Randomized non-parametric statistics report a drastic shift toward hyper-connectivity in the hM3D(Gq)-mCh group after clozapine injection (15 min bins). (**B**) Circos-plot showing the anatomical location of hyper-connected edges in response to LC activation ($p<0.05$, Network Based Statistics, FWE corrected). (**C**) Node Modulation Index (NMI), calculated as the averaged effect-size in each brain area (165 ROIs, based on the Allen Common Coordinate Framework). (**D**) Rendering of NMI in Allen MRI space, revealing a heterogeneous distribution across brain regions. (**E**) Bar plots representing all the ROIs with an NMI > 0.5 (moderate-to-strong effect). Full ROI list in Table S1. See also Figure S3 and Table S1.

Figure 4. Functional connectivity changes after LC-NE activation spatially correlate with adrenoceptor gene expression. Spearman correlation coefficients, Rho, and associated p-value (FDR corrected) between Node Modulation Index and the transcriptional maps of genes coding (**A**) adrenoceptors alpha 1; (**B**) adrenoceptors alpha 2; (**C**) adrenoceptors beta 1; (**D**) adrenoceptors beta 2. Gene expression data was obtained from the Allen Mouse Brain Atlas and measured using *in situ* hybridization. Transcriptional levels across a macroscopic cortical area were summarized and plotted as the mean ISH intensity across voxels of that brain area, or 'expression energy'. See also Figure S4 and Table S2.

Figure 5. Rapid changes in resting-state network connectivity after LC activation.
Voxel-wise dual-regression analysis of revealed clusters of significant 'group x time interactions' in 6/13 resting-state networks (p-value<0.05, TFCE corrected). A linear mixed model showed significant

network strength increases in the hM3Dq-mCh group compared to mCh control mice, after clozapine injection. Bar plots represent mean ± SEM. *=p<0.05, **=p<0.01 (FDR corrected).

Figure 6. NE and DA turnover induced by LC activation correlates with rs-fMRI data. (**A**) Outline of the tissue collection strategy following completion of fMRI scans. (CTX: cortex, HC: hippocampus, STR: striatum = caudate putamen) (**B**) Representative images of cFos expression in the LC after clozapine injection in hM3Dq-mCh or mCh mice. All scale bars: 50 μm. (**C-J**) Levels of monoaminergic neurotransmitters and their metabolites in the cortex, hippocampus and striatum. NE was reduced in all brain regions of hM3Dq-mCh mice relative to mCh controls (**C:** main effect of group: F(1,33)=42.48, p<0.0001), MHPG was increased (**D:** main effect of group F(1,33)=121.80, p<0.0001) and NE turnover ratio (MHPG/NE) was increased (**E:** main effect of group: F(1,33)=291.50, p<0.0001; two-way ANOVA with Sidak *post hoc* tests). Although there was no difference in the levels of DA (**F:** main effect for group F(1,33)=0.81, p=0.3748), its metabolite HVA was increased in the cortex and the hippocampus in hM3Dq-mCh mice (**G:** significant main effect for group F(1,11)=11.60, p=0.0059) and DOPAC was increased only in the hippocampus (**H:** significant main effect for group F(1,33)=22.13, p<0.0001;). The DA turnover ratios were only increased in the hippocampus, for both HVA/DA (**I:** main effect of group: F(1,33)=8.91, p=0.0053), and DOPAC/DA (**J:** main effect of group: F(1,33)=19.81, p<0.0001), two-way ANOVA with Sidak *post hoc* tests). (**K-M**) Correlation between FC changes and neurotransmitter levels in the cortex (**K),** in the hippocampus (**L**), and in the striatum (**M**). Circles correspond to mCh mice, filled circles to hM3Dq-mCh mice. *p<0.05, **p<0.01, ***p<0.001, ****p<0.0001. Data represent mean ± SEM. See also Figure S5 and Figure S6.

Figure 7. The dorsal striatum (caudate-putamen) is innervated by the LC. (**A**) Immunohistochemical localization of the norepinephrine transporter (NET) reveals noradrenergic axons in the caudate-putamen (arrows). (**B**) Magnification of the box in (**A**) showing NET+ axons (arrows). (**C**) A retro-AAV2 that expresses Cre-dependent mCherry was delivered to the dorsolateral caudate-putamen and resulted in mCherry+ neurons in the LC of DBH-iCre (n=3), but not in a wild type mouse (n=1, representative pictures from one animal shown, additional images for all mice in **Figure S11**). (**D**) Stereotactic delivery of a Cre-dependent retro-AAV2 virus expressing EGFP in the dorsolateral caudate-putamen resulted in EGFP+ LC neurons in a DBH-iCre mouse, but not in a wild type mouse. (**E**) Magnification of the box in (**D**) showing the axonal co-localization of NET and EGFP in the caudate putamen of a DBH-iCre animal. CTX=cortex; STR=striatum. See also Figure S7.

STAR Methods

CONTACT FOR REAGENT AND RESOURCE SHARING

Further information and requests for resources and reagents should be directed to and will be fulfilled by the Lead Contact, Johannes Bohacek (johannes.bohacek@hest.ethz.ch).

EXPERIMENTAL MODEL AND SUBJECT DETAILS

All experiments were conducted in accordance with the Swiss federal guidelines for the use of animals in research, and under licensing from the Zürich Cantonal veterinary office. Heterozygous C57BL/6-Tg(Dbh-icre)1Gsc mice(Parlato et al., 2007) were generously provided by Prof. Günther Schütz and kept in breeding trios with wild-type C57Bl/6J mice at the ETH Zurich animal facility (EPIC). Experiments were performed with heterozygous or wild-type healthy adult male and female mice that were maintained in IVC cages with food and water ad libitum, in a temperature- and humidity-controlled facility on a 12-hour reversed light-dark cycle (lights off: 9:15am; lights on: 9:15pm) and were housed in groups of 2-5 mice per cage. The behavioral effects of LC activation were first investigated in male and then reproduced and further characterized in female mice (Figure 1 and Figure S1). However the experiments on males and females were performed on separate days to avoid interference of odor cues. Thus, the results of males and females cannot be directly compared to investigate potential sex

differences, although the response in both sexes looks very similar. The experimenters were blind to the DREADD groups for all experiments, and all trials were randomized.

METHOD DETAILS

Stereotaxic brain injections

Viral vectors and viral vector plasmids were designed and produced by the Viral Vector Facility (VVF) of the Neuroscience Center Zurich. The viruses used had a physical titer of 6.0-6.5 x 10^{12} vg/ml. For virus delivery, 2- to 3-month-old mice were subjected to stereotactic brain injections. The mice were anesthetized with isoflurane and placed in a stereotaxic frame. For analgesia, animals received a subcutaneous injection of 2mg/kg Meloxicam and a local anesthetic (Emla cream; 5% lidocaine, 5% prilocaine) before and after surgery. A pneumatic injector (Narishige, IM-11-2) and calibrated microcapillaries (Sigma-Aldrich, P0549) were used to inject 1 µL of virus (either ssAAV-5/2-hSyn1-dlox-hM3D(Gq)_mCherry(rev)-dlox-WPRE-hGHp(A) or ssAAV-5/2-hSyn1-dlox-mCherry(rev)-dlox-WPRE-hGHp(A)) bilaterally into the locus coeruleus (coordinates from bregma: anterior/posterior -5.4 mm, medial/lateral +/-1.0 mm, dorsal/ventral -3.8 mm). For the retrograde AAV2 injection, 0.8 µL of ssAAV-retro/2-hEF1α-dlox-hChR2(H134R)_mCherry(rev)-dlox-WPRE-hGHp(A) or ssAAV-retro/2-hEF1a-dlox-EGFP(rev)-dlox-WPRE-bGHp(A) was delivered bilaterally to the dorsolateral site of the caudate-putamen (from bregma: anterior/posterior 0.86 mm, medial/lateral +/-1.8 mm, dorsal/ventral -3.2 mm). The health of the animals was evaluated by post-operative checks over the course of 3 consecutive days.

Pupil recordings

For pupil recordings we used a Raspberry Pi NoIR Camera Module V2 night vision camera, an infrared light source (Pi Supply Bright Pi - Bright White and IR camera light for Raspberry Pi) and a Raspberry Pi 3 Model B (Raspberry Pi Foundation, UK). Animals were anesthetized with isoflurane (4% induction, 1.5% maintenance), then an intraperitoneal catheter delivering PBS was placed and the video recording was initiated. After 2 minutes of baseline recording, 0.03 mg/kg clozapine (Sigma-Aldrich, Steinheim, Germany) was injected through the catheter and the video recording continued for another 8 minutes.

Behavioral testing

All experiments took place in testing rooms illuminated with red LED lights (637 nm), during the dark period of the light-dark cycle.

Open field test (OFT)

Open-field testing took place inside sound insulated, ventilated multi-conditioning chambers (MultiConditioning System, TSE Systems Ltd, Germany). The open field arena (45 cm (l) x 45 cm (w) x 40 cm (h)) consisted of four transparent Plexiglas walls and a light grey PVC floor. Mice were tested under dim lighting (4 Lux across the floor of the open field, provided by four equally spaced yellow overhead lights) with 75-77 dB of white noise playing through the speakers of each box, as described previously(Sturman et al., 2018). Animals were injected i.p. with 0.03 mg/kg clozapine (Sigma-Aldrich, Steinheim, Germany) and placed directly into the center of the open field. Tracking/recording was initiated upon first locomotion grid beam break, lasted for 30 minutes and was analyzed in 3-minute bins.

Light dark box (LDB)

For the light dark box testing, a box with a light and a dark compartment was placed inside sound insulated, ventilated multi-conditioning chambers (MultiConditioning System, TSE Systems Ltd, Germany). The light dark compartment (28cm (l) x 30 cm (w) x 25 cm (h)) consisted of transparent Plexiglas walls, while the dark compartment (16cm (l) x 30 cm (w) x 25 cm (h)) with black Plexiglas walls. The compartments were separated with a black Plexiglas dividing wall with a small central

opening (6.6cm (w) x 7cm (h)) to let the mouse move freely between compartments. The entire arena had a light grey PVC floor. Two white lights directly above the light compartment were used to light the arena (200 Lux in the light compartment, 0-1 lux in the dark compartment). 60-65 dB of white noise was played through the speakers of each box throughout testing. Animals were injected i.p. with 0.03 mg/kg clozapine (Sigma-Aldrich, Steinheim, Germany) and placed directly into the center of the light compartment. Tracking/recording was initiated upon first locomotion grid beam break, lasted for 30 minutes and was analyzed in 3-minute bins.

Rotarod test

To test motor function of mice during chemogenetic actication of LC, we tested them on a Rotarod (Accurotor Rota Rod, Accuscan Instruments, Inc.) accelerating from 4 to 40 rpm in 300 seconds. Mice were subjected in 5 trials/day for 3 consecutive days. The maximum duration of every trial was 5 minutes, and minimum 5 minutes break was given between trials. After a day of training, the mice were tested on the Rotarod on Day 2. On Day 3, mice were injected with 30μg/kg clozapine i.p. and immediately placed on the Rotarod.

Tissue collection and processing

Tissue collection for immunohistochemistry

When brain tissue was collected exclusively for immunohistochemistry, mice were deeply anesthetized with pentobarbital (150 mg/kg, i.p.) and perfused intracardially through the left ventricle for 2 minutes, with approximately 20 mL ice-cold PBS (pH 7.4). The brain was dissected, blocked and fixed for 2-3 hrs in ice-cold paraformaldehyde solution (4% PFA in PBS, pH 7.4). The tissue was rinsed with PBS and stored in a sucrose solution (30% sucrose in PBS) at 4°C, overnight. Then the tissue was frozen in tissue mounting medium (Tissue-Tek O.C.T Compound, Sakura Finetek Europe B.V., Netherlands), and sectioned coronally using a cryostat (Leica CM3050 S, Leica Biosystems Nussloch GmbH) into 40 μm thick sections. The sections were immediately transferred into ice-cold PBS.

Tissue collection for uHPLC and immunohistochemistry

When brain tissue was collected for both uHPLC and immunohistochemistry, mice were rapidly euthanized by cervical dislocation. The brain was first divided into an anterior and a posterior part with a single cut from a razorblade at the beginning of the cerebellum as shown in Figure 5A. The cortex (overlying the hippocampus), hippocampus and striatum were immediately dissected on an ice-cold glass surface, snap-frozen in liquid nitrogen and stored at -80°C until further processing for uHPLC. The posterior part including the locus coeruleus was fixed in 4% PFA for 2 hours, cryoprotected in a sucrose solution and frozen in mounting medium as described above for immunohistochemistry.

Brain illustrations were created with the Scalable Brain Atlas(Bakker et al., 2015; Lein et al., 2007).

Immunohistochemistry

For immunohistochemistry, brain sections were submerged in primary antibody solution containing 0.2% Triton X-100, and 2% normal goat serum in PBS, and were incubated at 4ºC under continuous agitation over 2 nights. Then the sections were washed 3 times in PBS for 10 minutes/wash, and transferred in secondary antibody solution containing 2% normal goat serum in PBS. After 3 more PBS washes, the sections were mounted onto glass slides (Menzel-Gläser SUPERFROST PLUS, Thermo Scientific), air-dried and coverslipped with Dako fluorescence mounting medium (Agilent Technologies). The primary antibodies used were: rabbit anti-mCherry (ab167453, Abcam, 1:1000), mouse anti-TH (22941, Immunostar, 1:1000), rabbit anti-cFos (226 003, Synaptic Systems, 1:5000), mouse anti-NET (NBP1-28665, Novus Biologicals, 1:1000), chicken anti-GFP (ab13970, Abcam. 1:1000). The secondary antibodies used were: goat anti-rabbit Alexa 546 (A11035, Thermo Fisher Scientific, 1:300), goat anti-mouse Alexa 488 (ab150113, Abcam, 1:300), goat anti-mouse Cy3 (115-165-003, Jackson ImmunoResearch, 1:300), goat anti-rabbit Alexa Fluor 488 (A-11008, Thermo Fisher Scientific, 1:500), goat anti-chicken Alexa Fluor 488 (A-11039, Thermo Fischer Scientific, 1:1000) and Nissl stain (N21483, NeuroTrace 640/660 Nissl stain, Thermo Fischer Scientific, 1:300).

Microscopy images were acquired in a confocal laser-scanning microscope (CLSM 880, Carl Zeiss AG, Germany), maintaining a pinhole aperture of 1.0 Airy Unit and image size 1024x1024 pixels. Images of LC were acquired using a Z-stack with a 20x objective and pixel size 0.59 μm. Images of the caudate putamen and the whole brain (sagittal plane) were acquired with the 20x (pixel size 0.59 μm) and the 10x (pixel size 1.19 μm) objective respectively, using a Z-stack and tiles. Images of axons were acquired with the 20x (pixel size 0.59 μm) or the 40x (pixel size 0.35 μm) objective.

MRI

Anesthesia

The levels of anesthesia and physiological parameters were monitored to obtain a reliable measurement of functional connectivity following established protocols(Grandjean et al., 2014; Zerbi et al., 2015). Briefly, anesthesia was induced with 4% isoflurane and the animals were endotracheally intubated and the tail vein cannulated. Mice were positioned on a MRI-compatible cradle, and artificially ventilated at 80 breaths per minute, 1:4 O_2 to air ratio, and 1.8 ml/h flow (CWE, Ardmore, USA). A bolus injection of muscle relaxant (pancuronium bromide, 0.2 mg/kg) was administered, and isoflurane was reduced to 1%. Throughout the experiment, mice received a continuous infusion of pancuronium bromide 0.4 mg/kg/h. Body temperature was monitored using a rectal thermometer probe, and maintained at 36.5 °C ± 0.5 during the measurements. The preparation of the animals did not exceed 15 minutes. In an additional experiment, mice were pre-treated with a bolus injection of medetomidine 0.05 mg/kg, followed by a continuous infusion at 0.1 mg/kg/h.

Data acquisition

Data acquisition was performed on a Biospec 70/16 small animal MR system (Bruker BioSpin MRI, Ettlingen, Germany) equipped with a cryogenic quadrature surface coil for signal detection (Bruker BioSpin AG, Fällanden, Switzerland). Standard adjustments included the calibration of the reference frequency power and the shim gradients using MapShim (Paravision v6.1). For anatomical assessment, a T2-weighted image is acquired (FLASH sequence, in-plane resolution of 0.05 × 0.02 mm, TE = 3.51, TR = 522ms). For functional connectivity acquisition, a standard gradient-echo echo planar imaging sequence (GE-EPI, repetition time TR=1s, echo time TE=15ms, in-plane resolution RES=0.22×0.2mm^2, number of slice NS=20, slice thickness ST=0.4 mm, slice gap=0.1mm) was applied to acquire 2280 volumes in 38 min. After 15 minutes of GE-EPI acquisition, a bolus of 0.03 mg/kg clozapine was intravenously injected to activate DREADDs.

Outlier Removal

All mice (hM3Dq-mCh n=11; mCh n=8) successfully completed both fMRI sessions. However, due to a fault in the ventilation system that artificially supports breathing after the MRI, three animals died after the second session (hM3Dq-mCh n=2; mCh n=1). For all the others, the time until conscious intention to move was 10.6±4 minutes. One animal (mCh group) was excluded from the rs-fMRI analysis because the preparation time exceeded 30 minutes (average time between anesthesia induction and start of the MRI scanning, including intubation and cannulation was 12.8±3 minutes). In the weeks between the second fMRI session and tissue collection for molecular analyses, 2 mice were found dead in their cage (n=1 from hM3Dq-mCh, and n=1 from mCh groups). Otherwise, no mice were excluded from any of the experiments.

Ultra-high performance liquid chromatography (uHPLC)

To quantify norepinephrinergic (NE; epinephrine; MHPG), dopaminergic (DA; DOPAC; HVA), and serotonergic (5-HT; 5-HIAA) compounds, a reversed-phase uHPLC system coupled with electrochemical detection (RP-uHPLC-ECD) was used (Alexys™ Neurotransmitter Analyzer, Antec Leyden, Zoeterwoude, Netherlands). In short, our previously validated RP-HPLC method with ion pairing chromatography was applied as described (Van Dam et al., 2014), albeit with minor modifications regarding the installed column (BEH C18 Waters column, 150 mm x 1mm, 1.7μm particle

size) and pump preference (LC110S pump, 497 bar; flow rate of 68µL/min), achieving the most optimal separation conditions in a RP-uHPLC setting. Levels of the monoamines and metabolites were calculated using Clarity software™ (DataApex Ltd., v6.2.0.208, 2015, Prague, Czech Republic).
Brain samples were defrosted to 4 °C and subsequently homogenized in cold 800µl sample buffer (50 mM citric acid, 50 mM phosphoric acid, 0.1 mM EDTA, 8 mM KCl and 1.8 mM octane-1-sulfonic acid sodium salt (OSA), adjusted to pH = 3.6), using a Bio-Gen PRO200 homogenizer (PRO Scientific Inc., Oxford, CT, USA; 60 s, 4°C). To remove excess proteins, 450 µl homogenate was transferred onto a 10,000 Da Amicon® Ultra 0.5 Centrifugal Filter (Millipore, Ireland) that had been pre-washed twice using 450µl sample buffer (centrifugation: 14,000 × g, 20 min, 4 °C). The Amicon® filter loaded with the homogenate was then centrifuged (14,000 × g, 20 min, 4°C). Finally, the filtrate was transferred into a polypropylene vial (0.3mL, Machery-Nagel GmbH & Co. KG, Germany) and automatically injected into the previously-mentioned uHPLC column by the Alexys™ AS110 sample injector.

QUANTIFICATION AND STATISTICAL ANALYSIS

Statistical details for every experiment are provided in the figure legends, where "n" represents number of animals per group. Statistical significance was defined as $p < 0.05$.

Quantification

Pupillometry

Pupil diameter was measured using a custom MATLAB (MathWorks, Natick, MA, USA) script. Frames were binarized and an ellipse-fitting algorithm was used to approximate the pupil size. Measurements after clozapine injection were then normalized to baseline (measurements before clozapine).

OFT and LDB

All output parameters of the OFT and LDB were quantified by the software of the MultiConditioning System (TSE Systems Ltd, Germany).

cFos expression

Confocal images were imported to Image J (Schneider et al., 2012) enabled by Fiji (Schindelin et al., 2012), and neurons (Nissl positive cells) expressing TH, cFos or both were counted manually.

Statistical analysis

GraphPad Prism 8.0 was used for statistical analyses for behavior, pupillometry, immunohistochemistry and uHPLC data. We used independent samples t-tests when comparing two independent groups, and paired-samples t-tests when comparing the same group twice. When comparing more than two groups, we used one-way ANOVAs if there was a single independent variable, or two-way ANOVAs for two-factorial designs (e.g. time x group). Significant main effects and interactions were analyzed using Sidak's post hoc tests.

Resting-state fMRI

Data pre-processing and analysis

Resting state fMRI datasets were de-spiked and artefacts were removed using an existing automated pipeline designed in FSL (https://fsl.fmrib.ox.ac.uk/fsl/), adapted for the mouse (Zerbi et al., 2015). This procedure includes ICA-based artefact removal, motion correction and regression. Thereafter, data sets were band-pass filtered (0.01-0.25 Hz), skull-stripped and normalized to the Allen Brain Institute reference atlas (http://mouse.brain-map.org/static/atlas) using ANTs v2.1 (picsl.upenn.edu/ANTS).
Two types of analyses were performed on this data to compare the influence of LC activation on functional connectivity; first, we employed an exploratory and data-driven ***connectome*** analysis to describe the temporal and spatial changes at the whole-brain level. Briefly, BOLD time series are extracted using a subset of ROIs from the Allen's Common Coordinate Framework (V3,

http://help.brain-map.org/download/attachments/2818169/MouseCCF.pdf), which consisted of 165 ROIs from isocortex, hippocampal formation, cortical subplate, striatum, pallidum, thalamus, hypothalamus, hindbrain and midbrain (full list available in **Table S1**). Connectivity couplings between all ROIs are measured using a regularized Pearson's correlation coefficient implemented in FSLNets, using sliding time windows of either 1 minute (**Figure 2**) or 15 minutes (**Figure 3**). ***T***he connectome matrices were fed into a nonparametric permutation testing with 5000 permutations to detect differences in edge strength (i.e. connectivity between two brain areas or nodes) between groups. The results were corrected for multiple comparisons with Network Based Statistics (NBS) toolbox, and considered significant at a $p<0.05$.

In our second analyses, we focused on changes in spatial patterns of correlated activity, also called ***resting-state networks*** (RSNs). We selected 15 meaningful RSNs from an independent cohort of n=15 mice. Please note that the motor network, the striatum network and the striato-motor network are highly correlated, thus we considered only the latter for the analysis and reduced the number of RSNs to 13. We performed a dual regression approach (Zuo et al., 2010) as described by (Zerbi et al., 2018). [Re-iterate thresholding how you have thresholded the data etc in case this information would be remove from the figure caption] With this approach, we derived an index of coupling strength (i.e. temporal synchronicity) of the voxels within each RSN, by averaging the Z-scores from the group-mean RSNs masks (thresholded at the 75th percentile). Group level statistics were performed in SPSS v22 using a Linear Mixed-Model, with the fixed factors DREADD-Group and Time (2-levels, repeated measure), and with the individual mice as the random factor. Corresponding contrasts were used for post-hoc pairwise comparisons (LSD). *P*-values were considered significant at $p<0.05$ after False Discovery Rate (FDR) correction for multiple comparisons between RSNs.

Gene expression

Gene expression data was obtained from the Allen Mouse Brain Atlas (AMBA) (Lein et al., 2007) using the Allen Software Development Kit (SDK, https://github.com/benfulcher/AllenSDK) (Fulcher et al., 2018). Gene expression data in the AMBA is measured using in situ hybridization from: (i) sagittal section experiments with high genome coverage, and (ii) coronal section replications for approximately 3500 genes with restricted expression patterns in the brain (11). Transcriptional levels of major neurotransmitters across a macroscopic cortical area were summarized as the 'expression energy' (the mean ISH intensity across voxels of that brain area) (Lein et al., 2007; Ng et al., 2009).

Correlation and multiple regression analyses.

Correlations between Node Modulation Index and gene expression data was conducted using Spearman's correlations. A null distribution of Spearman's rho values was obtained for each gene by shuffling NMI ROI labels 10.000 times in a MATLAB (MathWorks, Natick, MA, USA) using a script developed in-house. We also used Spearman partial correlation to find the relative importance of each gene subunit influencing NMI correlations. Transcriptional levels of genes within the same families (i.e. adrenergic, dopaminergic, cholinergic nicotinic) were not considered in the regression due to their strong co-expression. See supplementary Table 2 for details

DATA AND SOFTWARE AVAILABILITY

Resting-state fMRI dataset are available upon request to the authors

References

Aksenov, D.P., Li, L., Miller, M.J., Iordanescu, G., and Wyrwicz, A.M. (2015). Effects of Anesthesia on BOLD Signal and Neuronal Activity in the Somatosensory Cortex. J. Cereb. Blood Flow Metab. *35*, 1819–1826.

Antelman, S., and Caggiula, A. (1977). Norepinephrine-dopamine interactions and behavior. Science (80-.). *195*, 646–653.

Armbruster, B.N., Li, X., Pausch, M.H., Herlitze, S., and Roth, B.L. (2007). Evolving the lock to fit the key to create a family of G protein-coupled receptors potently activated by an inert ligand. Proc. Natl. Acad. Sci. *104*, 5163–5168.

Arnsten, A.F.T. (2009). Stress signalling pathways that impair prefrontal cortex structure and function. Nat. Rev. Neurosci. *10*, 410–422.

Aston-Jones, G. (2004). Locus Coeruleus, A5 and A7 Noradrenergic Cell Groups. Rat Nerv. Syst. 259–294.

Aston-Jones, G., and Cohen, J.D. (2005). An integrative theory of locus coeruleus-norepinephrine function: adaptive gain and optimal performance. Annu. Rev. Neurosci. *28*, 403–450.

Avery, M.C., and Krichmar, J.L. (2017). Neuromodulatory Systems and Their Interactions: A Review of Models, Theories, and Experiments. Front. Neural Circuits *11*, 1–18.

Bakker, R., Tiesinga, P., and Kötter, R. (2015). The Scalable Brain Atlas: Instant Web-Based Access to Public Brain Atlases and Related Content. Neuroinformatics *13*, 353–366.

Bangasser, D.A., and Valentino, R.J. (2014). Sex differences in stress-related psychiatric disorders: Neurobiological perspectives. Front. Neuroendocrinol. *35*, 303–319.

Bangasser, D.A., Eck, S.R., and Ordoñes Sanchez, E. (2019). Sex differences in stress reactivity in arousal and attention systems. Neuropsychopharmacology *44*, 129–139.

Barsegyan, A., Mirone, G., Ronzoni, G., Guo, C., Song, Q., van Kuppeveld, D., Schut, E.H.S., Atsak, P., Teurlings, S., McGaugh, J.L., et al. (2019). Glucocorticoid enhancement of recognition memory via basolateral amygdala-driven facilitation of prelimbic cortex interactions. Proc. Natl. Acad. Sci. 201901513.

Beas, B.S., Wright, B.J., Skirzewski, M., Leng, Y., Hyun, J.H., Koita, O., Ringelberg, N., Kwon, H.-B., Buonanno, A., and Penzo, M.A. (2018). The locus coeruleus drives disinhibition in the midline thalamus via a dopaminergic mechanism. Nat. Neurosci. *21*, 963–973.

Berridge, C.W., and Waterhouse, B.D. (2003). The locus coeruleus–noradrenergic system: modulation of behavioral state and state-dependent cognitive processes. Brain Res. Rev. *42*, 33–84.

Berton, O., and Nestler, E.J. (2006). New approaches to antidepressant drug discovery: beyond monoamines. Nat. Rev. Neurosci. *7*, 137–151.

Borodovitsyna, O., Joshi, N., and Chandler, D. (2018). Persistent Stress-Induced Neuroplastic Changes in the Locus Coeruleus/Norepinephrine System. Neural Plast. *2018*, 1–14.

Bouret, S., and Sara, S.J. (2002). Locus coeruleus activation modulates firing rate and temporal organization of odour-induced single-cell responses in rat piriform cortex. Eur. J. Neurosci. *16*, 2371–2382.

Bukhari, Q., Schroeter, A., and Rudin, M. (2018). Increasing isoflurane dose reduces homotopic correlation and functional segregation of brain networks in mice as revealed by resting-state fMRI. Sci. Rep. *8*, 1–12.

Bullmore, E., and Sporns, O. (2009). Complex brain networks: Graph theoretical analysis of structural and functional systems. Nat. Rev. Neurosci. *10*, 186–198.

Bylund, D.B., and Snyder, S.H. (1976). Beta adrenergic receptor binding in membrane preparations from mammalian brain. Mol. Pharmacol. *12*, 568–580.

Carter, M.E., Yizhar, O., Chikahisa, S., Nguyen, H., Adamantidis, A., Nishino, S., Deisseroth, K., and de Lecea, L. (2010). Tuning arousal with optogenetic modulation of locus coeruleus neurons. Nat. Neurosci. *13*, 1526–1533.

Corbetta, M., Patel, G., and Shulman, G.L. (2008). The Reorienting System of the Human Brain: From Environment to Theory of Mind. Neuron *58*, 306–324.

Crick, F.C., and Koch, C. (2005). What is the function of the claustrum? Philos. Trans. R. Soc. B Biol. Sci. *360*, 1271–1279.

Van Dam, D., Vermeiren, Y., Aerts, T., and De Deyn, P.P. (2014). Novel and sensitive reversed-phase high-pressure liquid chromatography method with electrochemical detection for the simultaneous and fast determination of eight biogenic amines and metabolites in human brain tissue. J. Chromatogr. A *1353*, 28–39.

Devoto, P., Flore, G., Saba, P., Fà, M., and Gessa, G.L. (2005a). Stimulation of the locus coeruleus elicits noradrenaline and dopamine release in the medial prefrontal and parietal cortex. J. Neurochem. *92*, 368–374.

Devoto, P., Flore, G., Saba, P., Fà, M., and Gessa, G.L. (2005b). Co-release of noradrenaline and dopamine in the cerebral cortex elicited by single train and repeated train stimulation of the locus coeruleus. BMC Neurosci.

6, 1–11.

Fitzgerald, J.M., DiGangi, J.A., and Phan, K.L. Functional Neuroanatomy of Emotion and Its Regulation in PTSD. Harv. Rev. Psychiatry *26*, 116–128.

Fortress, A.M., Hamlett, E.D., Vazey, E.M., Aston-Jones, G., Cass, W.A., Boger, H.A., and Granholm, A.-C.E. (2015). Designer receptors enhance memory in a mouse model of Down syndrome. J. Neurosci. *35*, 1343–1353.

Fulcher, B.D., and Fornito, A. (2016). A transcriptional signature of hub connectivity in the mouse connectome. Proc. Natl. Acad. Sci. *113*, 1435–1440.

Fulcher, B.D., Murray, J.D., Zerbi, V., and Wang, X.-J. (2018). Multimodal gradients across mouse cortex. 1–7.

Giorgi, A., Migliarini, S., Galbusera, A., Maddaloni, G., Mereu, M., Margiani, G., Gritti, M., Landi, S., Trovato, F., Bertozzi, S.M., et al. (2017). Brain-wide Mapping of Endogenous Serotonergic Transmission via Chemogenetic fMRI. Cell Rep. *21*, 910–918.

Gomez, J.L., Bonaventura, J., Lesniak, W., Mathews, W.B., Sysa-Shah, P., Rodriguez, L.A., Ellis, R.J., Richie, C.T., Harvey, B.K., Dannals, R.F., et al. (2017). Chemogenetics revealed: DREADD occupancy and activation via converted clozapine. Science (80-.). *503*, 503–507.

Grandjean, J., Schroeter, A., Batata, I., and Rudin, M. (2014). NeuroImage Optimization of anesthesia protocol for resting-state fMRI in mice based on differential effects of anesthetics on functional connectivity patterns. Neuroimage *102*, 838–847.

Grandjean, J., Azzinnari, D., Seuwen, A., Sigrist, H., Seifritz, E., Pryce, C.R., and Rudin, M. (2016). Chronic psychosocial stress in mice leads to changes in brain functional connectivity and metabolite levels comparable to human depression. Neuroimage *142*, 544–552.

Hara, M., Fukui, R., Hieda, E., Kuroiwa, M., Bateup, H.S., Kano, T., Greengard, P., and Nishi, A. (2010). Role of adrenoceptors in the regulation of dopamine/DARPP-32 signaling in neostriatal neurons. J. Neurochem. *113*, 1046–1059.

Hermans, E.J., van Marle, H.J.F., Ossewaarde, L., Henckens, M.J.A.G., Qin, S., van Kesteren, M.T.R., Schoots, V.C., Cousijn, H., Rijpkema, M., Oostenveld, R., et al. (2011). Stress-related noradrenergic activity prompts large-scale neural network reconfiguration. Science *334*, 1151–1153.

Hermans, E.J., Henckens, M.J.A.G., Joëls, M., and Fernández, G. (2014). Dynamic adaptation of large-scale brain networks in response to acute stressors. Trends Neurosci. *37*, 304–314.

van den Heuvel, M.P., and Hulshoff Pol, H.E. (2010). Exploring the brain network: a review on resting-state fMRI functional connectivity. Eur. Neuropsychopharmacol. *20*, 519–534.

Hirschberg, S., Li, Y., Randall, A., Kremer, E.J., Pickering, A.E., Kingdom, U., and Kingdom, U. (2017). Functional dichotomy in spinal- vs prefrontal-projecting locus coeruleus modules splits descending noradrenergic analgesia from ascending aversion & anxiety in rats. Elife 1–26.

Ihalainen, J.A., Riekkinen, P., and Feenstra, M.G.P. (1999). Comparison of dopamine and noradrenaline release in mouse prefrontal cortex, striatum and hippocampus using microdialysis. Neurosci. Lett. *277*, 71–74.

Isingrini, E., Perret, L., Rainer, Q., Amilhon, B., Guma, E., Tanti, A., Martin, G., Robinson, J., Moquin, L., Marti, F., et al. (2016). Resilience to chronic stress is mediated by noradrenergic regulation of dopamine neurons. Nat. Neurosci. *19*, 560–563.

Joëls, M., and Baram, T.Z. (2009). The neuro-symphony of stress. Nat. Rev. Neurosci. *10*, 459–466.

Jorm, C.M., and Stamford, J.A. (1993). Actions of the hypnotic anaesthetic, dexmedetomidine, on noradrenaline release and cell firing in rat locus coeruleus slices. Br. J. Anaesth. *71*, 447–449.

Kawahara, H., Kawahara, Y., and Westerink, B.H.C. (2001). The noradrenaline-dopamine interaction in the rat medial prefrontal cortex studied by multi-probe microdialysis. Eur. J. Pharmacol. *418*, 177–186.

Kempadoo, K.A., Mosharov, E. V, Choi, S.J., Sulzer, D., and Kandel, E.R. (2016). Dopamine release from the locus coeruleus to the dorsal hippocampus promotes spatial learning and memory. Proc. Natl. Acad. Sci. U. S. A. 201616515.

Lakhlani, P.P., MacMillan, L.B., Guo, T.Z., McCool, B. a, Lovinger, D.M., Maze, M., and Limbird, L.E. (1997). Substitution of a mutant α2a-adrenergic receptor via "hit and run" gene targeting reveals the role of this subtype in sedative, analgesic, and anesthetic-sparing responses in vivo. Proc Natl Acad Sci U S A. *94*, 9950–9955.

Lee, S.H., and Dan, Y. (2012). Neuromodulation of Brain States. Neuron *76*, 109–222.

Lein, E.S., Hawrylycz, M.J., Ao, N., Ayres, M., Bensinger, A., Bernard, A., Boe, A.F., Boguski, M.S., Brockway, K.S., Byrnes, E.J., et al. (2007). Genome-wide atlas of gene expression in the adult mouse brain. Nature *445*, 168–176.

Li, L.L., Feng, X., Zhou, Z., Zhang, H., Shi, Q., Lei, Z., Shen, P., Yang, Q., Zhao, B., Chen, S., et al. (2018). Stress Accelerates Defensive Responses to Looming in Mice and Involves a Locus Coeruleus-Superior Colliculus Projection. Curr. Biol. *28*, 1–13.

Liberzon, I., and Phan, K.L. (2003). Brain-imaging studies of posttraumatic stress disorder. CNS Spectr. *8*, 641–650.

Liu, Y., Rodenkirch, C., Moskowitz, N., Schriver, B., and Wang, Q. (2017). Dynamic Lateralization of Pupil Dilation Evoked by Locus Coeruleus Activation Results from Sympathetic, Not Parasympathetic, Contributions. Cell Rep. *20*, 3099–3112.

Lohani, S., Poplawsky, A.J., Kim, S.G., and Moghaddam, B. (2017). Unexpected global impact of VTA dopamine neuron activation as measured by opto-fMRI. Mol. Psychiatry *22*, 585–594.

Magalhães, R., Barrière, D.A., Novais, A., Marques, F., Marques, P., Cerqueira, J., Sousa, J.C., Cachia, A., and Boumezbeur, F. (2018). The dynamics of stress : a longitudinal MRI study of rat brain structure and connectome. 1998–2006.

Mana, M.J., and Grace, A.A. (1997). Chronic cold stress alters the basal and evoked electrophysiological activity of rat locus coeruleus neurons. Neuroscience *81*, 1055–1064.

Manaye, K.F., McIntire, D.D., Mann, D.M.A., and German, D.C. (1995). Locus coeruleus cell loss in the aging human brain: A non-random process. J. Comp. Neurol. *358*, 79–87.

Markicevic, M., Fulcher, B.D., Lewis, C., Helmchen, F., Rudin, M., Zerbi, V., Wenderoth, N., Marija, A., Fulcher, B.D., Lewis, C., et al. (2018). Cortical excitation:inhibition imbalance causes network specific functional hypoconnectivity: a DREADD-fMRI study. BioRxiv 492108.

van Marle, H.J.F., Hermans, E.J., Qin, S., and Fernández, G. (2010). Enhanced resting-state connectivity of amygdala in the immediate aftermath of acute psychological stress. Neuroimage *53*, 348–354.

Mason, S.T., and Fibiger, H.C. (1979). Regional topography within noradrenergic locus coeruleus as revealed by retrograde transport of horseradish peroxidase. J. Comp. Neurol. *187*, 703–724.

Mather, M., Clewett, D., Sakaki, M., and Harley, C.W. (2016). Norepinephrine ignites local hotspots of neuronal excitation: How arousal amplifies selectivity in perception and memory. Behav. Brain Sci. *39*.

McCall, J.G., Al-Hasani, R., Siuda, E.R., Hong, D.Y., Norris, A.J., Ford, C.P., and Bruchas, M.R. (2015). CRH Engagement of the Locus Coeruleus Noradrenergic System Mediates Stress-Induced Anxiety. Neuron *87*, 605–620.

McCall, J.G., Siuda, E.R., Bhatti, D.L., Lawson, L.A., McElligott, Z.A., Stuber, G.D., and Bruchas, M.R. (2017). Locus coeruleus to basolateral amygdala noradrenergic projections promote anxiety-like behavior. Elife *6*, 1–23.

Models, A. (2005). Neuroanatomical Phenotyping in the Mouse: The Dopaminergic System. Vet. Pathol. *773*, 753–773.

Mulvey, B., Bhatti, D.L., Gyawali, S., Lake, A.M., Kriaucionis, S., Ford, C.P., Bruchas, M.R., Heintz, N., and Dougherty, J.D. (2018). Molecular and Functional Sex Differences of Noradrenergic Neurons in the Mouse Locus Coeruleus. Cell Rep. *23*, 2225–2235.

Murphy, P.R., O'Connell, R.G., O'Sullivan, M., Robertson, I.H., and Balsters, J.H. (2014). Pupil diameter covaries with BOLD activity in human locus coeruleus. Hum. Brain Mapp. *35*, 4140–4154.

Naegeli, C., Zeffiro, T., Piccirelli, M., Jaillard, A., Weilenmann, A., Hassanpour, K., Schick, M., Rufer, M., Orr, S.P., and Mueller-Pfeiffer, C. (2018). Locus Coeruleus Activity Mediates Hyperresponsiveness in Posttraumatic Stress Disorder. Biol. Psychiatry *83*, 254–262.

Ng, L., Bernard, A., Lau, C., Overly, C.C., Dong, H.W., Kuan, C., Pathak, S., Sunkin, S.M., Dang, C., Bohland, J.W., et al. (2009). An anatomic gene expression atlas of the adult mouse brain. Nat. Neurosci. *12*, 356–362.

Nicholas, A.P., Hökfelt, T., and Pieribone, V.A. (1996). The distribution and significance of CNS adrenoceptors examined with in situ hybridization. Trends Pharmacol. Sci. *17*, 245–255.

van Oort, J., Tendolkar, I., Hermans, E.J., Mulders, P.C., Beckmann, C.F., Schene, A.H., Fernández, G., and van Eijndhoven, P.F. (2017). How the brain connects in response to acute stress: A review at the human brain systems level. Neurosci. Biobehav. Rev. *83*, 281–297.

Palacios, J., and Kuhar, M. (1980). Beta-adrenergic-receptor localization by light microscopic autoradiography. Science (80-.). *208*, 1378–1380.

Parlato, R., Otto, C., Begus, Y., Stotz, S., and Schütz, G. (2007). Specific ablation of the transcription factor CREB in sympathetic neurons surprisingly protects against developmentally regulated apoptosis. Development *134*, 1663–1670.

Paschalis, A., Churchill, L., Marina, N., Kasymov, V., Gourine, A., and Ackland, G. (2009). β1-Adrenoceptor distribution in the rat brain: An immunohistochemical study. Neurosci. Lett. *458*, 84–88.

Pietrzak, R.H., Gallezot, J.-D., Ding, Y.-S., Henry, S., Potenza, M.N., Southwick, S.M., Krystal, J.H., Carson, R.E., and Neumeister, A. (2013). Association of Posttraumatic Stress Disorder With Reduced In Vivo Norepinephrine Transporter Availability in the Locus Coeruleus. JAMA Psychiatry *70*, 1199.

Pisani, A., Pisani, A., Bonsi, P., Bonsi, P., Centonze, D., Centonze, D., Martorana, A., Martorana, A., Fusco, F.,

Fusco, F., et al. (2003). Activation of beta1-adrenoceptors excites striatal cholinergic interneurons through a cAMP-dependent, protein kinase-independent pathway. J. Neurosci. *23*, 5272–5282.

Preller, K.H., Burt, J.B., Ji, J.L., Schleifer, C.H., Adkinson, B.D., Stämpfli, P., Seifritz, E., Repovs, G., Krystal, J.H., Murray, J.D., et al. (2018). Changes in global and thalamic brain connectivity in LSD-induced altered states of consciousness are attributable to the 5-HT2A receptor. Elife *7*, 1–31.

Ramos, B.P., and Arnsten, A.F.T. (2007). Adrenergic pharmacology and cognition : Focus on the prefrontal cortex. *113*, 523–536.

Ramos, B.P., Colgan, L., Nou, E., Ovadia, S., Wilson, S.R., and Arnsten, A.F.T. (2005). The beta-1 adrenergic antagonist, betaxolol, improves working memory performance in rats and monkeys. Biol. Psychiatry *58*, 894–900.

Ramos, B.P., Colgan, L.A., Nou, E., and Arnsten, A.F.T. (2008). B2 Adrenergic Agonist, Clenbuterol, Enhances Working Memory Performance in Aging Animals. Neurobiol. Aging *29*, 1060–1069.

Reimer, J., McGinley, M.J., Liu, Y., Rodenkirch, C., Wang, Q., McCormick, D.A., and Tolias, A.S. (2016). Pupil fluctuations track rapid changes in adrenergic and cholinergic activity in cortex. Nat. Commun. *7*, 13289.

Reisine, T.D., Nagy, J.I., Beaumont, K., Fibiger, H.C., and Yamamura, H.I. (1979). The localization of receptor binding sites in the substantia nigra and striatum of the rat. Brain Res. *177*, 241–252.

Roeder, T. (2005). TYRAMINE AND OCTOPAMINE: Ruling Behavior and Metabolism. Annu. Rev. Entomol. *50*, 447–477.

Roelofs, T.J.M., Verharen, J.P.H., van Tilborg, G.A.F., Boekhoudt, L., van der Toorn, A., de Jong, J.W., Luijendijk, M.C.M., Otte, W.M., Adan, R.A.H., and Dijkhuizen, R.M. (2017). A novel approach to map induced activation of neuronal networks using chemogenetics and functional neuroimaging in rats: A proof-of-concept study on the mesocorticolimbic system. Neuroimage *156*, 109–118.

Rommelfanger, K.S., Mitrano, D.A., Smith, Y., and Weinshenker, D. (2009). Light and electron microscopic localization of alpha-1 adrenergic receptor immunoreactivity in the rat striatum and ventral midbrain. Neuroscience *158*, 1530–1540.

Rosazza, C., and Minati, L. (2011). Resting-state brain networks: Literature review and clinical applications. Neurol. Sci. *32*, 773–785.

Roth, B.L. (2016). DREADDs for Neuroscientists. Neuron *89*, 683–694.

Rubinov, M., Ypma, R.J.F., Watson, C., and Bullmore, E.T. (2015). Wiring cost and topological participation of the mouse brain connectome. Proc. Natl. Acad. Sci. *112*, 10032–10037.

Sara, S.J., and Bouret, S. (2012). Orienting and Reorienting: The Locus Coeruleus Mediates Cognition through Arousal. Neuron *76*, 130–141.

Schallert, T., Whishaw, I.Q., Ramirez, V.D., and Teitelbaum, P. (1978). 6-hydroxydopamine and anticholinergic drugs. Science *202*, 1216–1217.

Schindelin, J., Arganda-Carreras, I., Frise, E., Kaynig, V., Longair, M., Pietzsch, T., Preibisch, S., Rueden, C., Saalfeld, S., Schmid, B., et al. (2012). Fiji: an open-source platform for biological-image analysis. Nat. Methods *9*, 676–682.

Schneider, C.A., Rasband, W.S., and Eliceiri, K.W. (2012). NIH Image to ImageJ: 25 years of image analysis. Nat. Methods *9*, 671–675.

Schroeter, S., Apparsundaram, S., Wiley, R.G., Miner, L.H., Sesack, S.R., and Blakely, R.D. (2000). Immunolocalization of the Cocaine- and l-Norepinephrine Transporter. *232*, 211–232.

Schwarz, L.A., and Luo, L. (2015). Organization of the locus coeruleus-norepinephrine system. Curr. Biol. *25*, R1051–R1056.

Seeley, W.W., Menon, V., Schatzberg, A.F., Keller, J., Glover, G.H., Kenna, H., Reiss, A.L., and Greicius, M.D. (2007). Dissociable Intrinsic Connectivity Networks for Salience Processing and Executive Control. J. Neurosci. *27*, 2349–2356.

Seo, D., Jia, Z., Lacadie, C.M., Tsou, K.A., Bergquist, K., and Sinha, R. (2011). Sex differences in neural responses to stress and alcohol context cues. Hum. Brain Mapp. *32*, 1998–2013.

Shine, J.M., Bissett, P.G., Bell, P.T., Koyejo, O., Balsters, J.H., Gorgolewski, K.J., Moodie, C.A., and Poldrack, R.A. (2016). The Dynamics of Functional Brain Networks: Integrated Network States during Cognitive Task Performance. Neuron *92*, 544–554.

Shine, J.M., Breakspear, M., Bell, P.T., Ehgoetz Martens, K., Shine, R., Koyejo, O., Sporns, O., and Poldrack, R.A. (2019). Human cognition involves the dynamic integration of neural activity and neuromodulatory systems. Nat. Neurosci.

Sinha, R., Lacadie, C., Skudlarski, P., and Wexler, B.E. (2004). Neural circuits underlying emotional distress in humans. Ann. N. Y. Acad. Sci. *1032*, 254–257.

Smith, C.C., and Greene, R.W. (2012). CNS Dopamine Transmission Mediated by Noradrenergic Innervation. J. Neurosci. *32*, 6072–6080.

Sturman, O., Germain, P.-L., and Bohacek, J. (2018). Exploratory rearing: a context- and stress-sensitive behavior recorded in the open-field test. Stress *21*, 443–452.

Swanson, L.W., and Hartman, B.K. (1975). The central adrenergic system. An immunofluorescence study of the location of cell bodies and their efferent connections in the rat utilizing dopamine-B-hydroxylase as a marker. J. Comp. Neurol. *163*, 467–505.

Takeuchi, T., Duszkiewicz, A.J., Sonneborn, A., Spooner, P.A., Yamasaki, M., Watanabe, M., Smith, C.C., Fernández, G., Deisseroth, K., Greene, R.W., et al. (2016). Locus coeruleus and dopaminergic consolidation of everyday memory. Nature *537*, 357–362.

Tervo, D.G.R., Hwang, B.Y., Viswanathan, S., Gaj, T., Lavzin, M., Ritola, K.D., Lindo, S., Michael, S., Kuleshova, E., Ojala, D., et al. (2016). A Designer AAV Variant Permits Efficient Retrograde Access to Projection Neurons. Neuron *92*, 372–382.

Totah, N.K., Neves, R.M., Panzeri, S., Logothetis, N.K., and Eschenko, O. (2018a). The Locus Coeruleus Is a Complex and Differentiated Neuromodulatory System. Neuron *99*, 1055–1068.e6.

Totah, N.K.B., Logothetis, N.K., and Eschenko, O. (2018b). Noradrenergic ensemble-based modulation of cognition over multiple timescales. Brain Res.

Uematsu, A., Tan, B.Z., Ycu, E.A., Cuevas, J.S., Koivumaa, J., Junyent, F., Kremer, E.J., Witten, I.B., Deisseroth, K., and Johansen, J.P. (2017). Modular organization of the brainstem noradrenaline system coordinates opposing learning states. Nat. Neurosci. *20*, 1602–1611.

Usher, M., Cohen, J.D., Servan-Schreiber, D., Rajkowski, J., and Aston-Jones, G. (1999). The role of locus coeruleus in the regulation of cognitive performance. Science (80-.). *283*, 549–554.

Vaisvaser, S., Lin, T., Admon, R., Podlipsky, I., Greenman, Y., Stern, N., Fruchter, E., Wald, I., Pine, D.S., Tarrasch, R., et al. (2013). Neural traces of stress: cortisol related sustained enhancement of amygdala-hippocampal functional connectivity. Front. Hum. Neurosci. *7*, 1–11.

Valentino, R.J., and Van Bockstaele, E. (2008). Convergent regulation of locus coeruleus activity as an adaptive response to stress. Eur. J. Pharmacol. *583*, 194–203.

Vermeiren, Y., and De Deyn, P.P. (2017). Targeting the norepinephrinergic system in Parkinson's disease and related disorders: The locus coeruleus story. Neurochem. Int. *102*, 22–32.

Weinshenker, D. (2018). Long Road to Ruin: Noradrenergic Dysfunction in Neurodegenerative Disease. Trends Neurosci. *41*, 211–223.

Yang, G.J., Murray, J.D., Wang, X.-J., Glahn, D.C., Pearlson, G.D., Repovs, G., Krystal, J.H., and Anticevic, A. (2016). Functional hierarchy underlies preferential connectivity disturbances in schizophrenia. Proc. Natl. Acad. Sci. *113*, E219–E228.

Zerbi, V., Grandjean, J., Rudin, M., and Wenderoth, N. (2015). Mapping the mouse brain with rs-fMRI: An optimized pipeline for functional network identification. Neuroimage *123*, 11–21.

Zerbi, V., Ielacqua, G.D., Markicevic, M., Haberl, M.G., Ellisman, M.H., A-Bhaskaran, A., Frick, A., Rudin, M., and Wenderoth, N. (2018). Dysfunctional Autism Risk Genes Cause Circuit-Specific Connectivity Deficits With Distinct Developmental Trajectories. Cereb. Cortex *28*, 2495–2506.

Zuo, X.N., Kelly, C., Adelstein, J.S., Klein, D.F., Castellanos, F.X., and Milham, M.P. (2010). Reliable intrinsic connectivity networks: Test-retest evaluation using ICA and dual regression approach. Neuroimage *49*, 2163–2177.

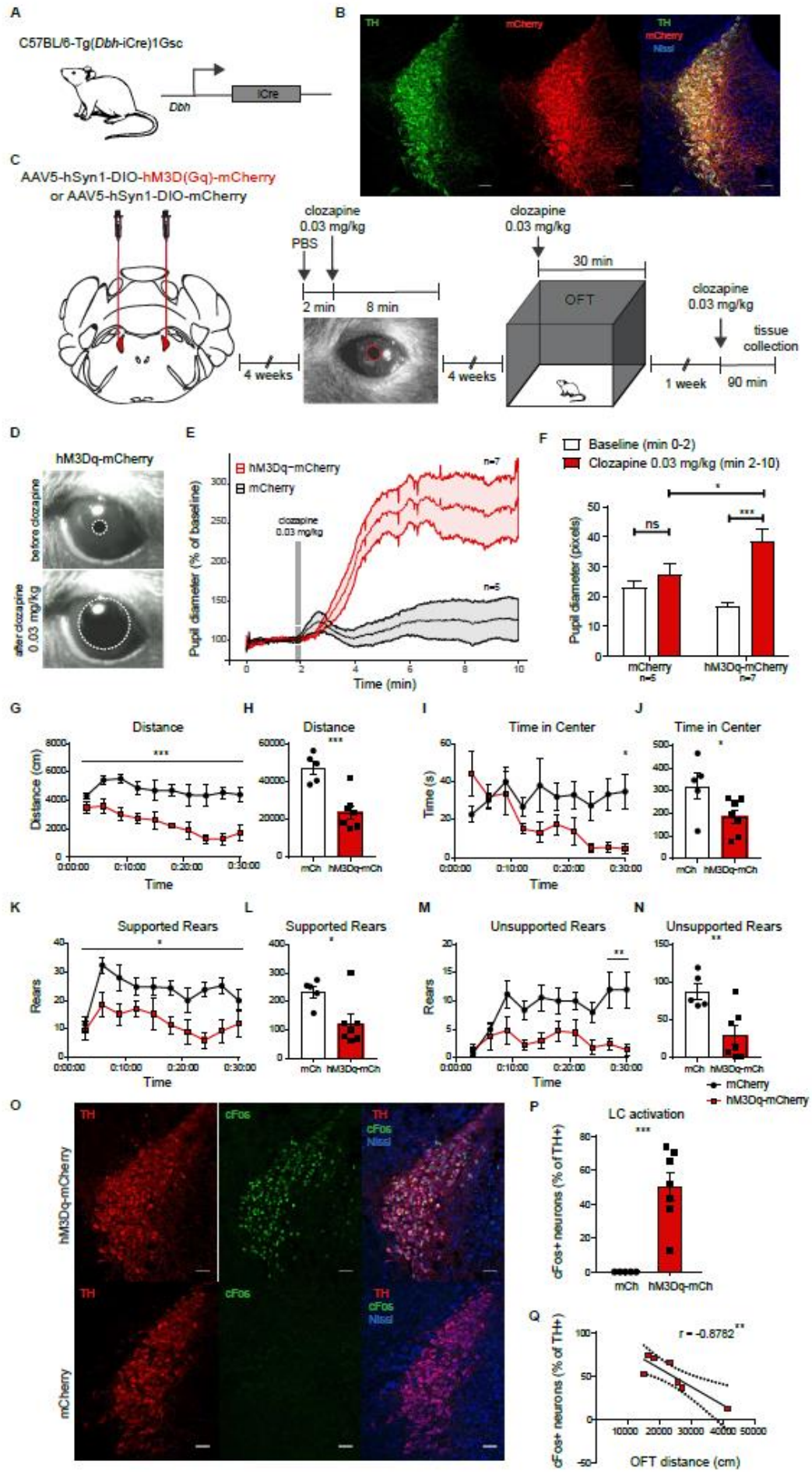
A
C57BL/6-Tg(Dbh-iCre)1Gsc
Dbh
iCre
B
TH
mCherry
TH
mCherry
Nissl
C
AAV5-hSyn1-DIO-hM3D(Gq)-mCherry
or AAV5-hSyn1-DIO-mCherry
clozapine
0.03 mg/kg
PBS
2 min
8 min
4 weeks
4 weeks
clozapine
0.03 mg/kg
30 min
OFT
clozapine
0.03 mg/kg
tissue
collection
1 week
90 min
D
hM3Dq-mCherry
before clozapine
after clozapine
0.03 mg/kg
E
hM3Dq-mCherry
mCherry
clozapine
0.03 mg/kg
n=7
n=5
Pupil diameter (% of baseline)
Time (min)
F
Baseline (min 0-2)
Clozapine 0.03 mg/kg (min 2-10)
ns
***
*
Pupil diameter (pixels)
mCherry
n=5
hM3Dq-mCherry
n=7
G
Distance
***
Distance (cm)
Time
H
Distance
***
mCh
hM3Dq-mCh
I
Time in Center
*
Time (s)
Time
J
Time in Center
*
mCh
hM3Dq-mCh
K
Supported Rears
*
Rears
Time
L
Supported Rears
*
mCh
hM3Dq-mCh
M
Unsupported Rears
**
Rears
Time
N
Unsupported Rears
**
mCh
hM3Dq-mCh
mCherry
hM3Dq-mCherry
O
hM3Dq-mCherry
mCherry
TH
cFos
TH
cFos
Nissl
P
LC activation
***
cFos+ neurons (% of TH+)
mCh
hM3Dq-mCh
Q
r = -0.8782**
cFos+ neurons (% of TH+)
OFT distance (cm)

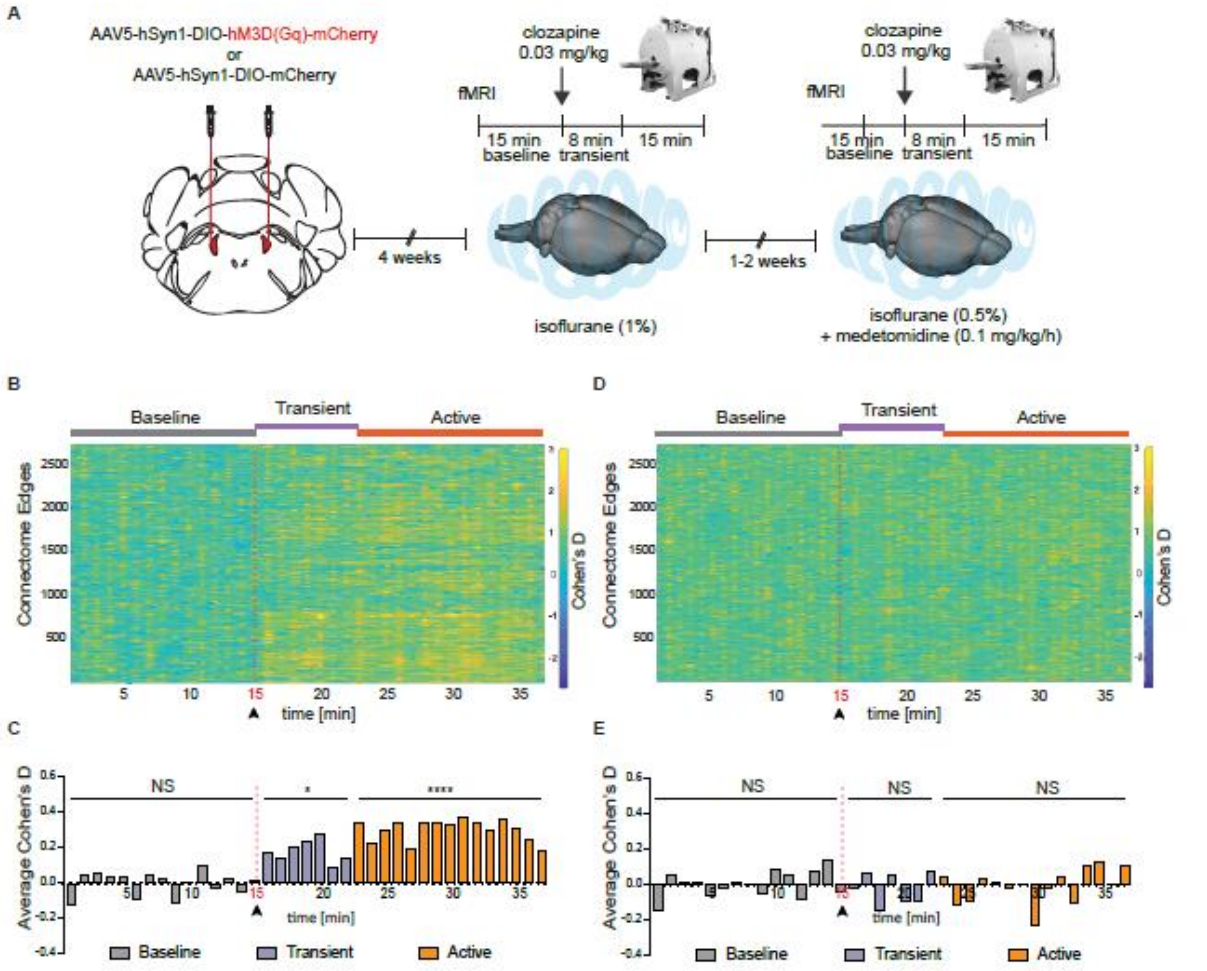
A
AAV5-hSyn1-DIO-hM3D(Gq)-mCherry
or
AAV5-hSyn1-DIO-mCherry
4 weeks
clozapine
0.03 mg/kg
fMRI
15 min
baseline
8 min
transient
15 min
isoflurane (1%)
1-2 weeks
clozapine
0.03 mg/kg
fMRI
15 min
baseline
8 min
transient
15 min
isoflurane (0.5%)
+ medetomidine (0.1 mg/kg/h)
B
Baseline
Transient
Active
Connectome Edges
Cohen's D
time [min]
D
Baseline
Transient
Active
Connectome Edges
Cohen's D
time [min]
C
Average Cohen's D
NS
*
****
time [min]
Baseline
Transient
Active
E
Average Cohen's D
NS
NS
NS
time [min]
Baseline
Transient
Active

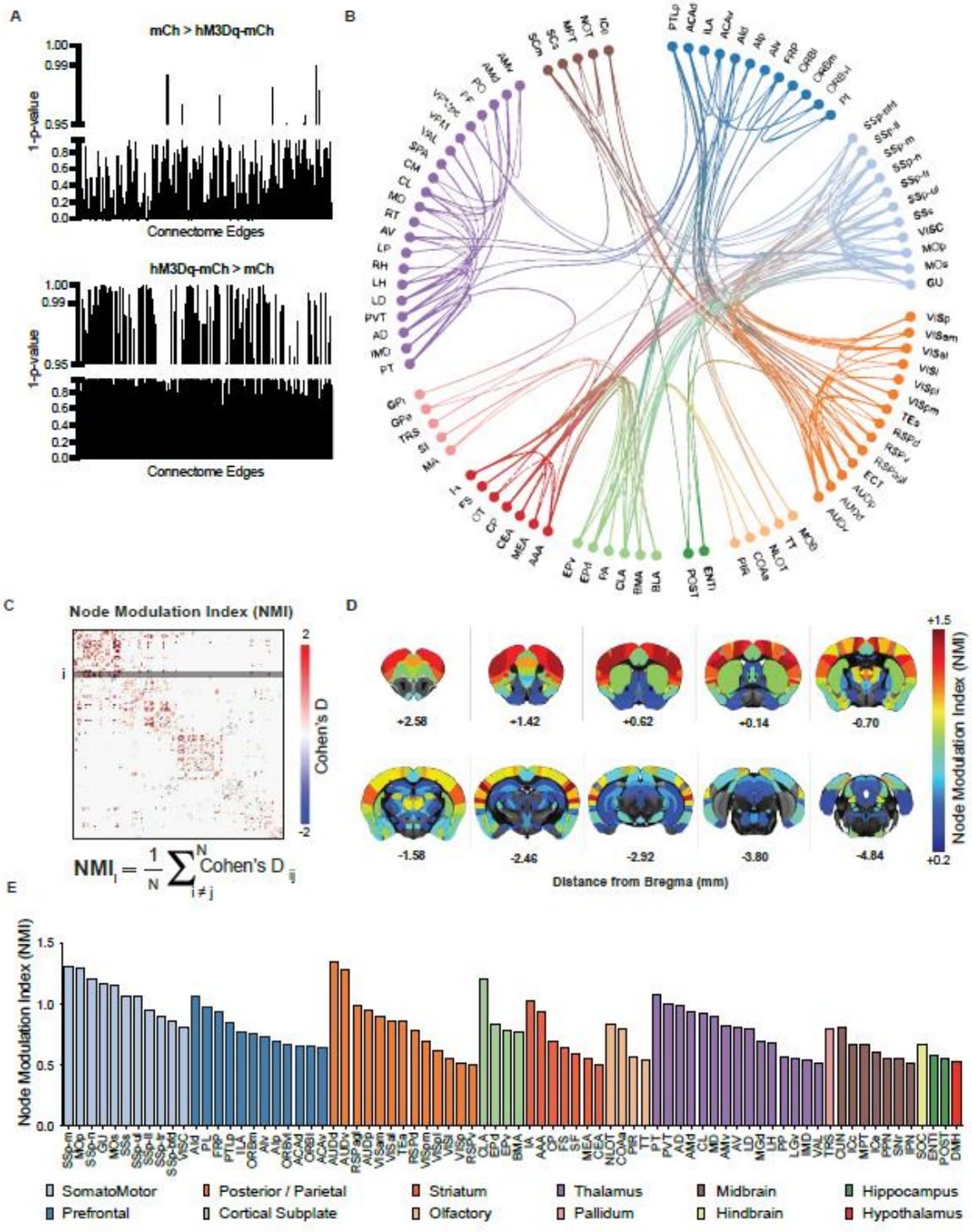
A
mCh > hM3Dq-mCh
1-p-value
Connectome Edges
hM3Dq-mCh > mCh
1-p-value
Connectome Edges
B
C
Node Modulation Index (NMI)
Cohen's D
NMI_i = 1/N Σ_{i≠j}^{N} Cohen's D_ij
D
+2.58
+1.42
+0.62
+0.14
-0.70
-1.58
-2.46
-2.92
-3.80
-4.84
Distance from Bregma (mm)
Node Modulation Index (NMI)
E
Node Modulation Index (NMI)
SomatoMotor
Prefrontal
Posterior / Parietal
Cortical Subplate
Striatum
Olfactory
Thalamus
Pallidum
Midbrain
Hindbrain
Hippocampus
Hypothalamus

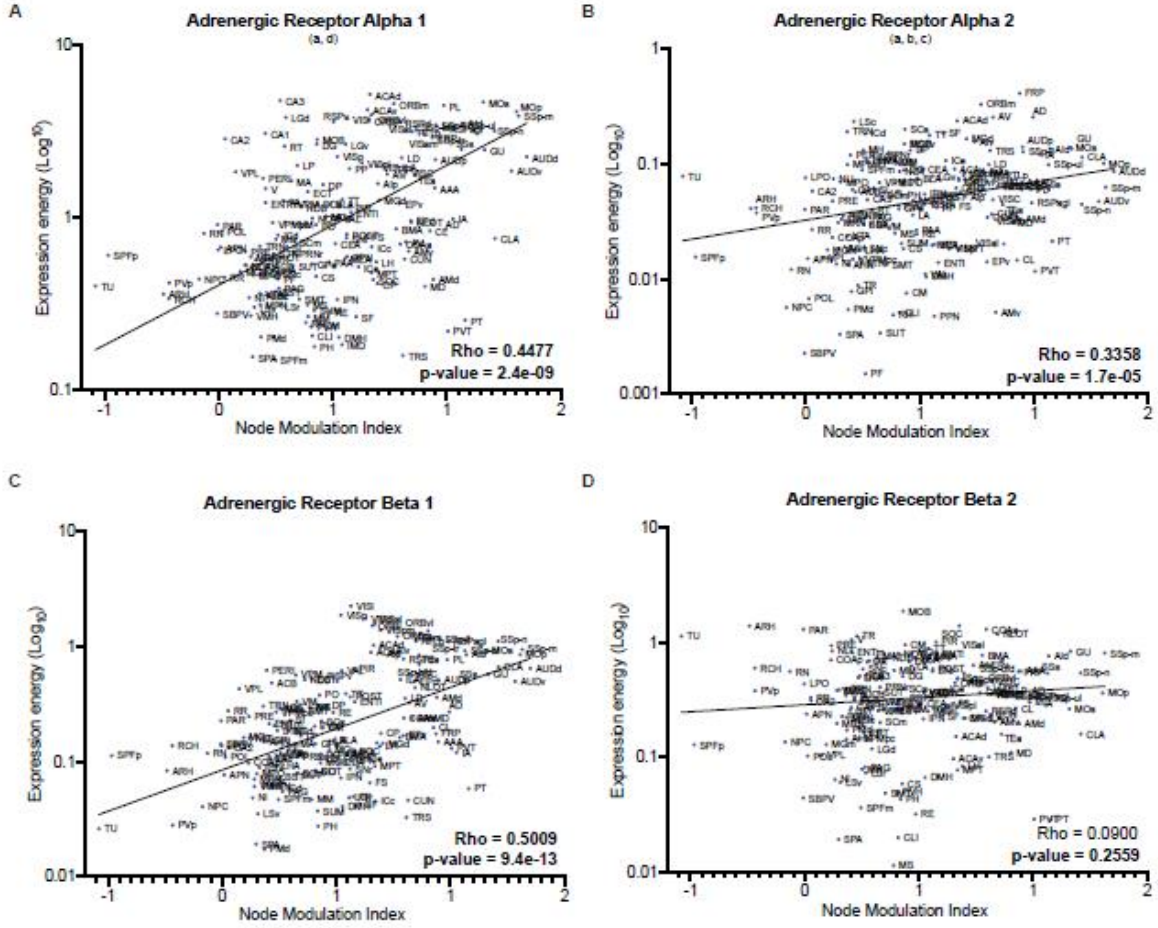
A
Adrenergic Receptor Alpha 1
(a, d)
Expression energy (Log10)
Node Modulation Index
Rho = 0.4477
p-value = 2.4e-09
B
Adrenergic Receptor Alpha 2
(a, b, c)
Expression energy (Log10)
Node Modulation Index
Rho = 0.3358
p-value = 1.7e-05
C
Adrenergic Receptor Beta 1
Expression energy (Log10)
Node Modulation Index
Rho = 0.5009
p-value = 9.4e-13
D
Adrenergic Receptor Beta 2
Expression energy (Log10)
Node Modulation Index
Rho = 0.0900
p-value = 0.2559

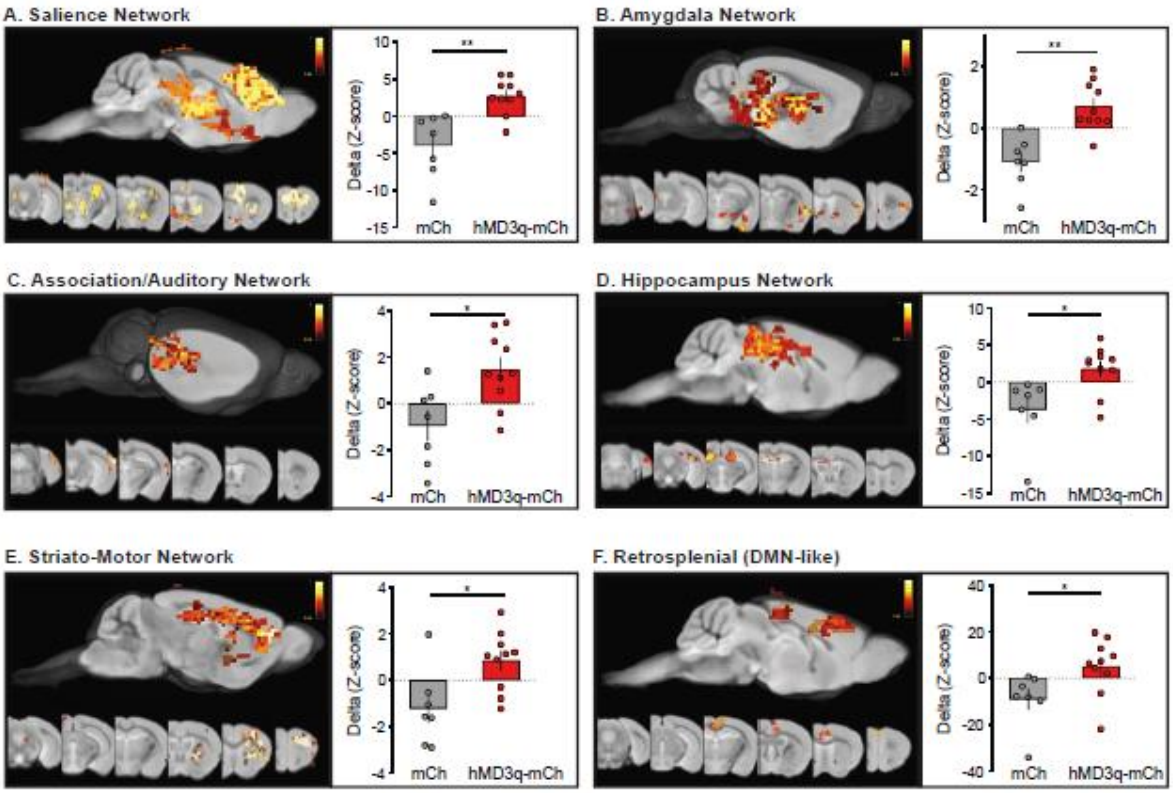
A. Salience Network
B. Amygdala Network
C. Association/Auditory Network
D. Hippocampus Network
E. Striato-Motor Network
F. Retrosplenial (DMN-like)
Delta (Z-score)
mCh
hMD3q-mCh

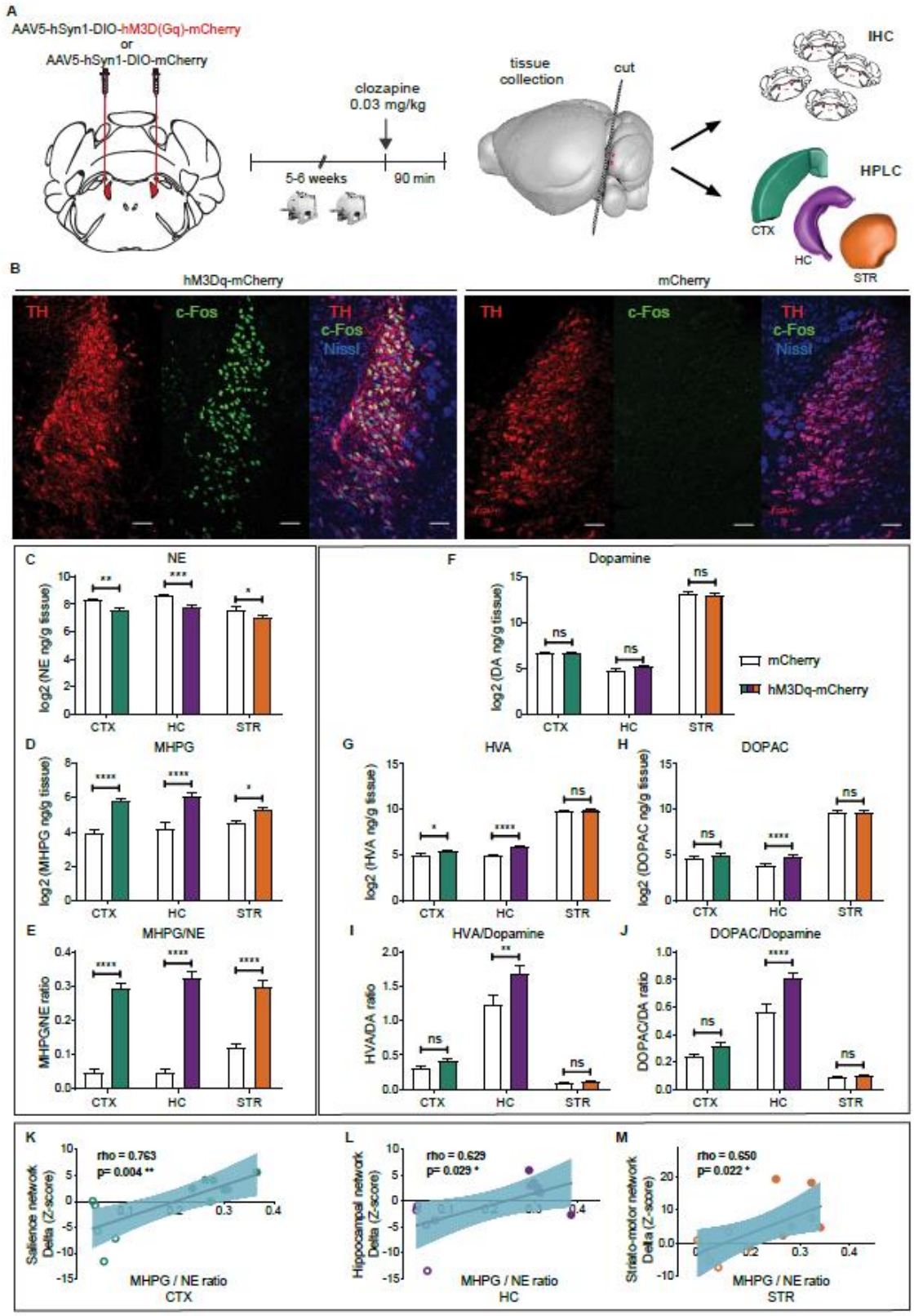
A
AAV5-hSyn1-DIO-hM3D(Gq)-mCherry
or
AAV5-hSyn1-DIO-mCherry
clozapine
0.03 mg/kg
5-6 weeks
90 min
tissue
collection
cut
IHC
HPLC
CTX
HC
STR
B
hM3Dq-mCherry
mCherry
TH
c-Fos
Nissl
C
NE
log2 (NE ng/g tissue)
D
MHPG
log2 (MHPG ng/g tissue)
E
MHPG/NE
MHPG/NE ratio
F
Dopamine
log2 (DA ng/g tissue)
mCherry
hM3Dq-mCherry
G
HVA
log2 (HVA ng/g tissue)
H
DOPAC
log2 (DOPAC ng/g tissue)
I
HVA/Dopamine
HVA/DA ratio
J
DOPAC/Dopamine
DOPAC/DA ratio
K
rho = 0.763
p= 0.004 **
Salience network
Delta (Z-score)
MHPG / NE ratio
CTX
L
rho = 0.629
p= 0.029 *
Hippocampal network
Delta (Z-score)
MHPG / NE ratio
HC
M
rho = 0.650
p= 0.022 *
Striato-motor network
Delta (Z-score)
MHPG / NE ratio
STR

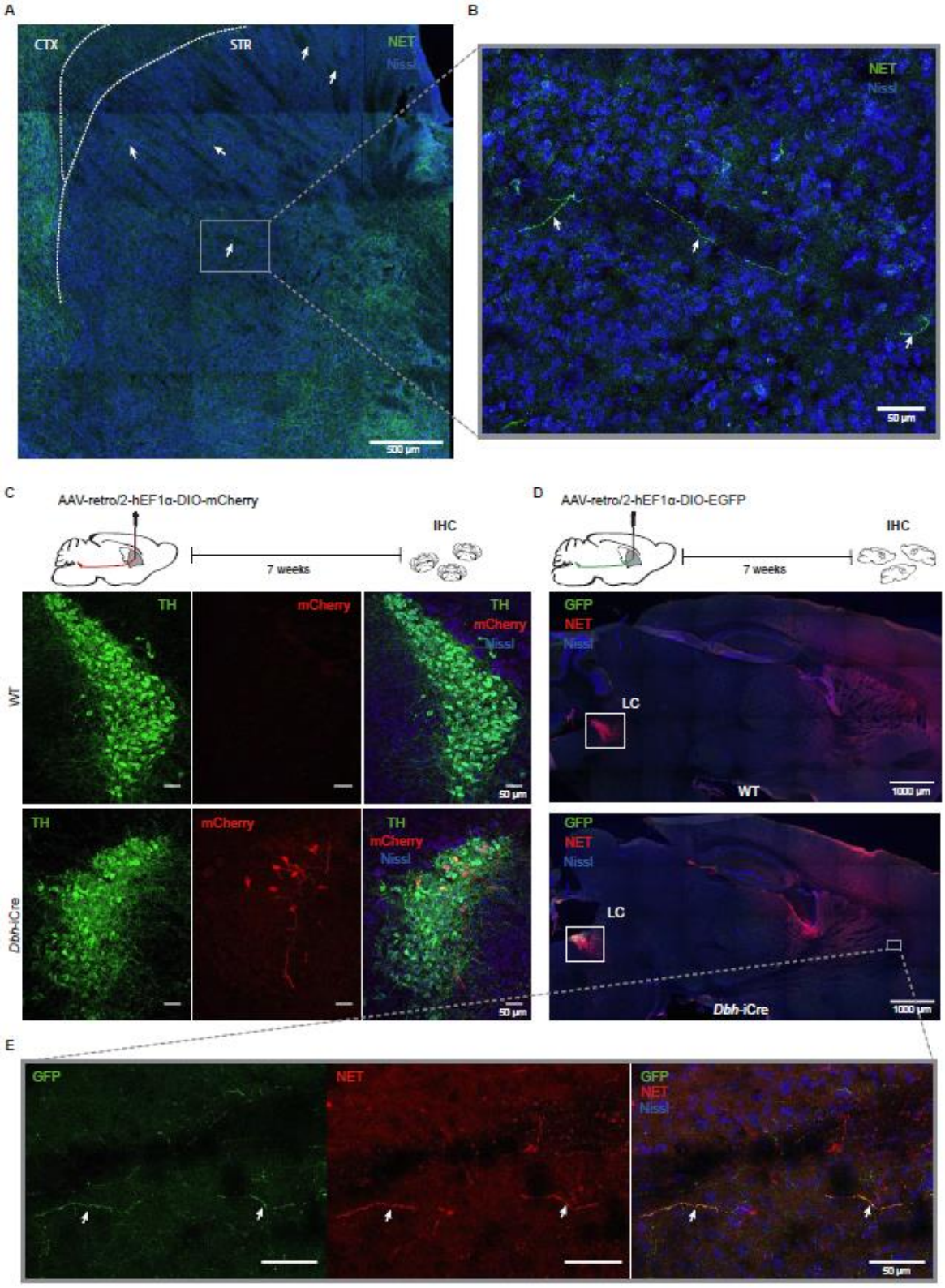
A
CTX
STR
NET
Nissl
500 μm
B
NET
Nissl
50 μm
C
AAV-retro/2-hEF1α-DIO-mCherry
IHC
7 weeks
WT
Dbh-iCre
TH
mCherry
Nissl
50 μm
D
AAV-retro/2-hEF1α-DIO-EGFP
IHC
7 weeks
GFP
NET
Nissl
LC
WT
Dbh-iCre
1000 μm
E
GFP
NET
Nissl
50 μm

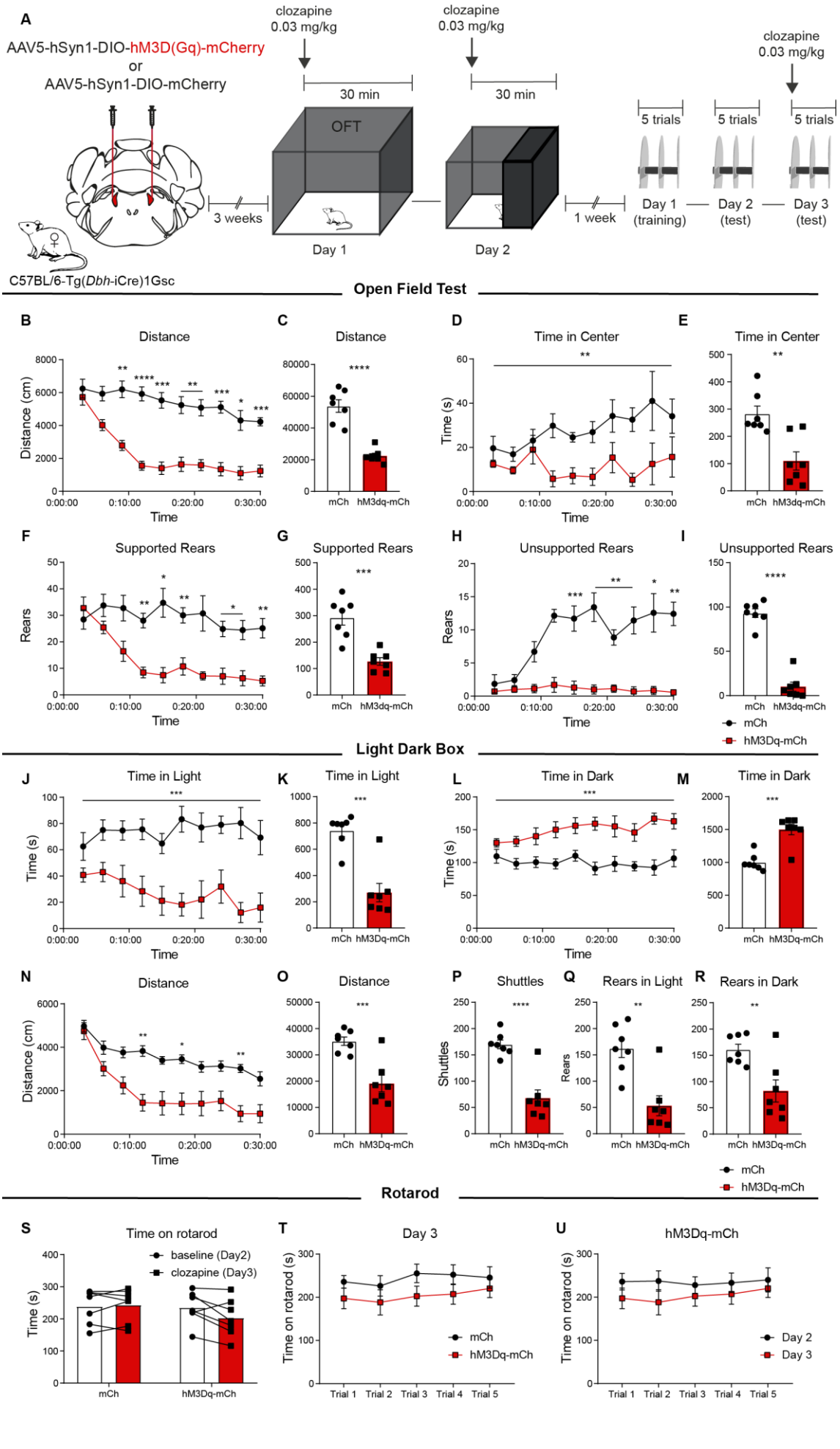
A
AAV5-hSyn1-DIO-hM3D(Gq)-mCherry
or
AAV5-hSyn1-DIO-mCherry
C57BL/6-Tg(Dbh-iCre)1Gsc
3 weeks
clozapine
0.03 mg/kg
30 min
OFT
Day 1
clozapine
0.03 mg/kg
30 min
Day 2
1 week
5 trials
Day 1
(training)
5 trials
Day 2
(test)
clozapine
0.03 mg/kg
5 trials
Day 3
(test)
Open Field Test
B
Distance
Distance (cm)
Time
C
Distance
mCh
hM3dq-mCh
D
Time in Center
Time (s)
Time
E
Time in Center
mCh
hM3dq-mCh
F
Supported Rears
Rears
Time
G
Supported Rears
mCh
hM3dq-mCh
H
Unsupported Rears
Rears
Time
I
Unsupported Rears
mCh
hM3dq-mCh
mCh
hM3Dq-mCh
Light Dark Box
J
Time in Light
Time (s)
Time
K
Time in Light
mCh
hM3Dq-mCh
L
Time in Dark
Time (s)
Time
M
Time in Dark
mCh
hM3Dq-mCh
N
Distance
Distance (cm)
Time
O
Distance
mCh
hM3Dq-mCh
P
Shuttles
Shuttles
mCh
hM3Dq-mCh
Q
Rears in Light
Rears
mCh
hM3Dq-mCh
R
Rears in Dark
mCh
hM3Dq-mCh
mCh
hM3Dq-mCh
Rotarod
S
Time on rotarod
baseline (Day2)
clozapine (Day3)
Time (s)
mCh
hM3Dq-mCh
T
Day 3
Time on rotarod (s)
mCh
hM3Dq-mCh
Trial 1
Trial 2
Trial 3
Trial 4
Trial 5
U
hM3Dq-mCh
Time on rotarod (s)
Day 2
Day 3
Trial 1
Trial 2
Trial 3
Trial 4
Trial 5

Figure S1. Related to Figure 1. (**A**) Diagram showing the time-course of behavioral tests after virus delivery in the LC of female DBH-iCre mice. (**B-I**) Mice were placed in the OFT directly after clozapine injection for 30 minutes. Mice expressing hM3Dq-mCh travelled less distance compared to mice expressing only mCh (**B, C:** main effect of group: $F(1,12)=53.71$, $p<0.0001$, interaction: $F(9,108)=6.32$, $p<0.0001$, two-way ANOVA with Sidak *post hoc* tests), spent less time in the center (**D, E:** main effect of group $F(1,12)=15.81$, $p=0.0018$, two-way ANOVA) and performed fewer supported rears (**F, G:** main effect of group $F(1,12)=27.46$, $p=0.0002$, interaction: $F(9,108)=4.24$, $p=0.0001$, two-way ANOVA with Sidak *post hoc* tests) and unsupported rears (**H, I:** main effect of group: $F(1,12)=137.9$, $p<0.0001$, interaction: $F(9,108)=5.26$, $p<0.0001$, two-way ANOVA with Sidak *post hoc* tests). (**J-R**) Mice were placed in the light dark box directly after clozapine injection for 30 minutes. Mice expressing hM3Dq-mCh spent less time in the light compartment in comparison to mCh controls (**J, K:** main effect of group: $F(1,12)=31.44$, $p=0.0001$, two-way ANOVA), more time in the dark compartment (**L, M:** main effect of group: $F(1,12)=28.75$, $p=0.0002$, two-way ANOVA), and travelled less distance (**N, O:** main effect of group: $F(1,12)=20.65$, $p=0.0007$, interaction: $F(9,108)=2.67$, $p=0.0072$, two-way ANOVA with Sidak *post hoc* tests). (**P-R**) Compared to mCh controls, hM3Dq-mCh mice also performed fewer shuttles between the light and the dark compartment (**P:** $t(12)=5.81$, $p<0.0001$, unpaired t test) and fewer rears in both compartments (**Q:** $t(12)=4.26$, $p=0.0011$, **R:** $t(12)=3.36$, $p=0.0057$, unpaired t test). (**S-U**) To assess gross motor function we trained the same mice on the Rotarod (Day 1, 5 trials) and tested them at baseline (Day 2, 5 trials) and immediately after clozapine injection (Day 3, 5 trials). The average performance from all trials of hM3Dq-mCh mice was slightly lower, not significantly different from mCh controls (**S:** main effect of group: $F(1,12)=2.61$, $p=0.1318$, interaction virus x group: $F(1,12)=4.61$, $p=0.0528$, two-way ANOVA). On Day 3, the performance of hM3Dq-mCh and mCh mice was not significantly different over the course of 5 trials (**T:** main effect of group: $F(1,12)=1.80$, $p=0.2040$, interaction trial x group: $F(4,48)=0.45$, $p=0.7743$, two-way ANOVA) and the performance of hM3Dq-mCh was not different between Day 2 and Day 3 over the course of 5 trials (**U:** main effect of group: $F(1,12)=1.18$, $p=0.2982$, interaction trial x group: $F(4,48)=0.46$, $p=0.7667$). *$p<0.05$, **$p<0.01$, ***$p<0.001$, ****$p<0.0001$. Data represent mean ± SEM

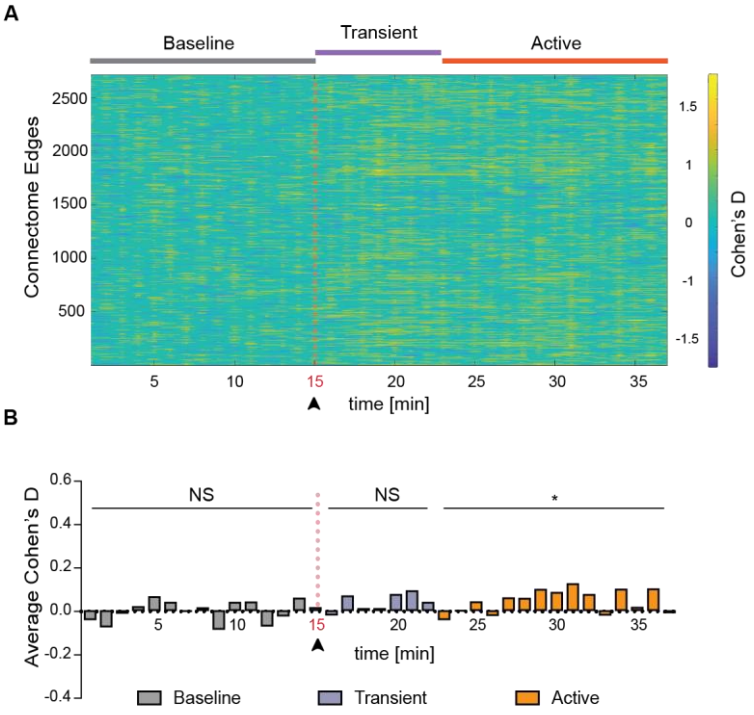

Figure S2. Related to Figure 2. Minor FC changes between anesthesia with 1% isoflurane versus anesthesia with 0.5% isoflurane + medetomidine. Effect-size (Cohen's D) analysis of Functional Connectivity (FC) is shown for single-edges (n=2724) between mCh mice (n=7) under two anesthesia conditions (see methods) (**A**) and for the average across all edges (**B**). The distribution of the data reveals a reduction of connectivity in multiple edges in the "1% isoflurane"-condition compared to the "0.5% isoflurane + medetomidine"-condition, about 30 minutes after the start of the session (Wilcoxon two-tailed test: p=0.9780 for baseline period, p=0.0781 for transient period and p=0.0181 for active period). The average net-effect of anesthesia is approximately 7 times smaller than the effect of LC-NE DREADD activation.

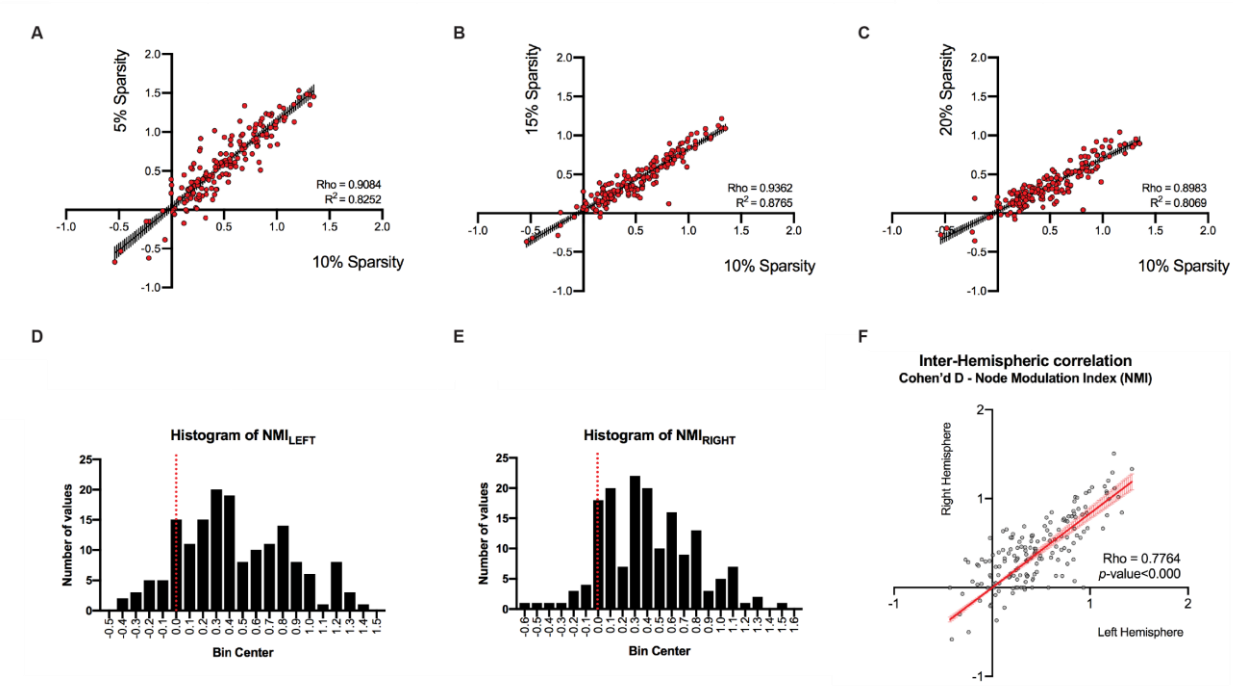

Figure S3. Related to Figure 3. (**A-C**) The Node Modulation Index (NMI) effect size is a robust index and correlates at different connectome sparsity-thresholds. The NMI effect size between mCh (n=7) and mCh-hM3Dq (n=11) under 1% isoflurane anesthesia is calculated at different sparsity thresholds (5%, 15%, 20%) of the connectome matrix. In each case, the resulting indices were highly linearly correlated (Pearson's correlation, *p*-value < 0.0001). (**D-F**) Coherent FC changes in the left and right hemisphere after LC-NE activation. Right-skewed distribution plots of Node Modulation Index effect size (Cohen's D) in the left (**D**) and in the right (**E**) hemispheres, demonstrating hyper-connectivity in both hemispheres. (**F**) The NMI measured in the left hemisphere shows positive linear correlation with respect to right hemisphere NMI (Pearson Rho=0.7764, p<0.0001). Data from mCh (n=7) and mCh-hM3Dq (n=11) under 1% isoflurane

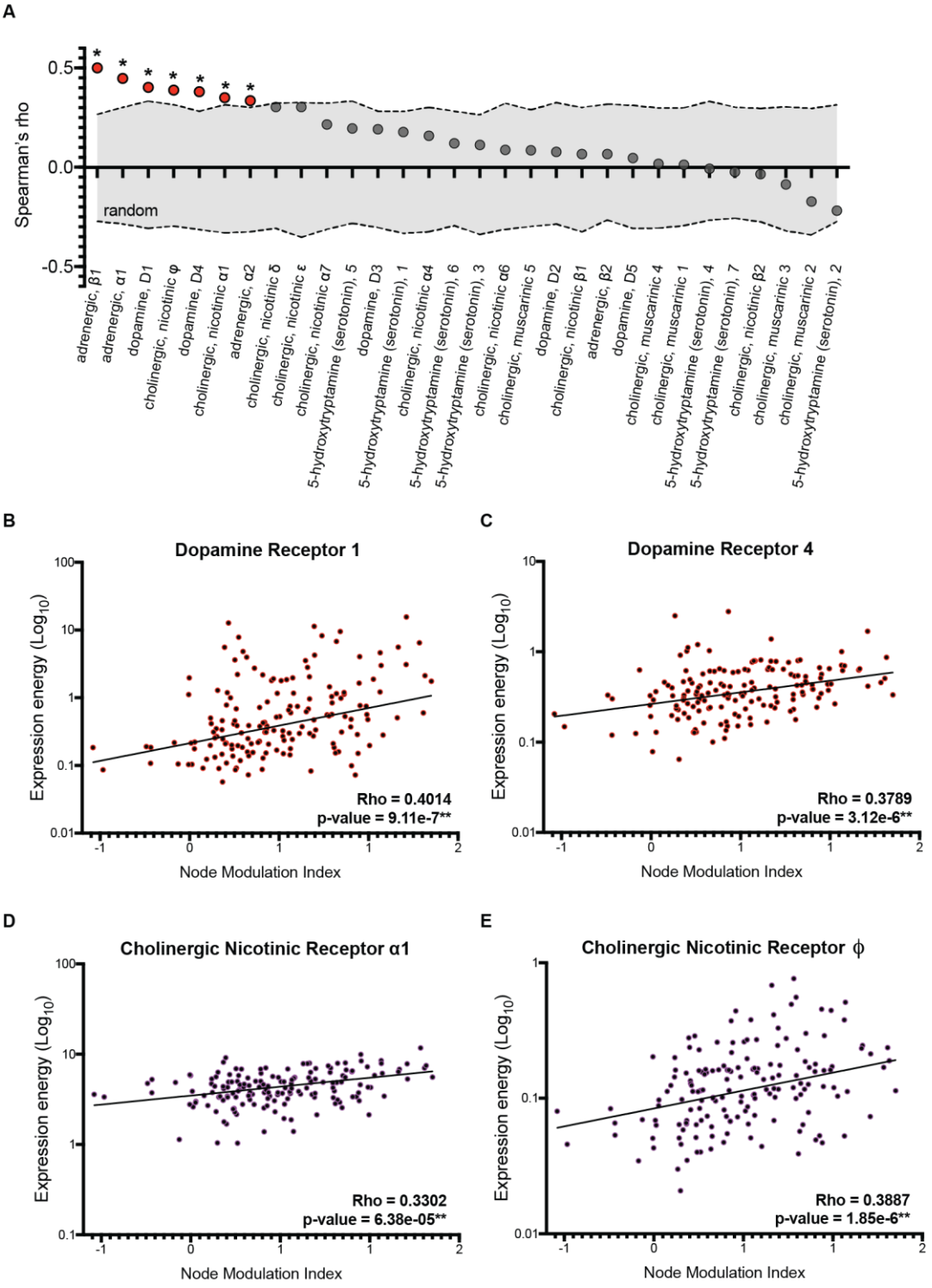

Figure S4. Related to Figure 4. Node Modulation Index maps correlate with dopamine D1, D4 and cholinergic nicotinic Φ and α1 receptor gene-transcript maps. (**A**) Spearman correlation coefficients, Rho, between Node Modulation Index (NMI) and gene-transcript maps for Adrenergic, Cholinergic, Dopaminergic and Serotonergic receptors were compared to a distribution of 100.000 randomized shuffled NMI labels. Whilst the highest correlation was achieved by adrenergic β1 and α1 receptor maps, we found a significant correlation and associated p-value (FDR corrected) between NMI and the transcriptional maps of genes coding dopaminergic receptor subunits 1 and 4 (**B-C**) and cholinergic nicotinic Φ and α1 (**D-E**). None of the transcriptional maps of cholinergic muscarinic nor serotonin receptors show significant correlation with the NMI.

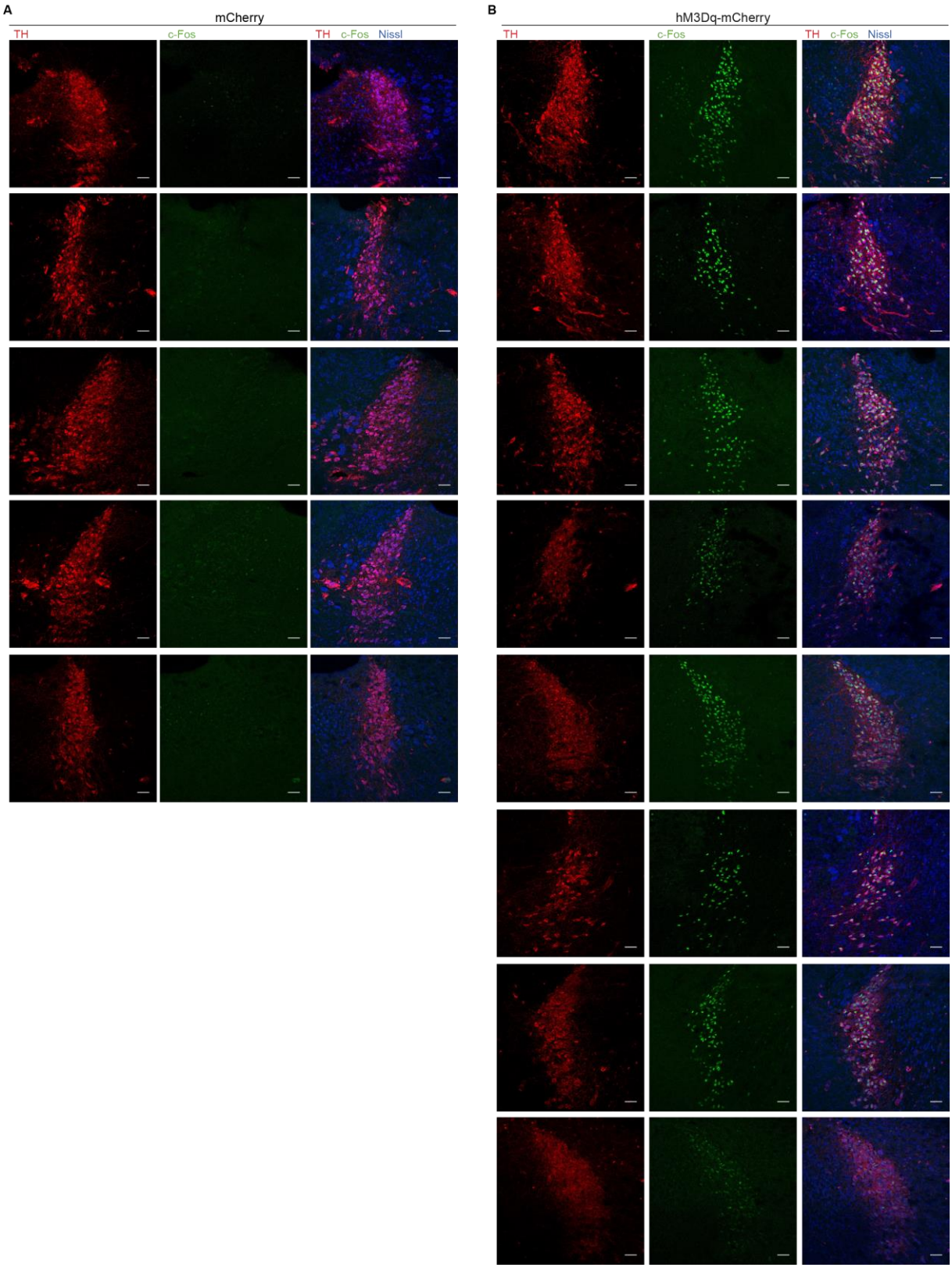

Figure S5. Related to Figure 6. Representative LC images of every mouse used for the fMRI scans. Every row shows 3 images from one mouse, stained for TH (left), cFos (middle), and the merged picture including a Nissl stain (right). Tissue was collected 90 minutes after 0.03mg/kg clozapine injection, and cFos is activated in all mice expressing hM3Dq-mCh (**B**), but not in mCh controls (**A**). Tissue collected as described in Figure 5. All scale bars: 50 μm.

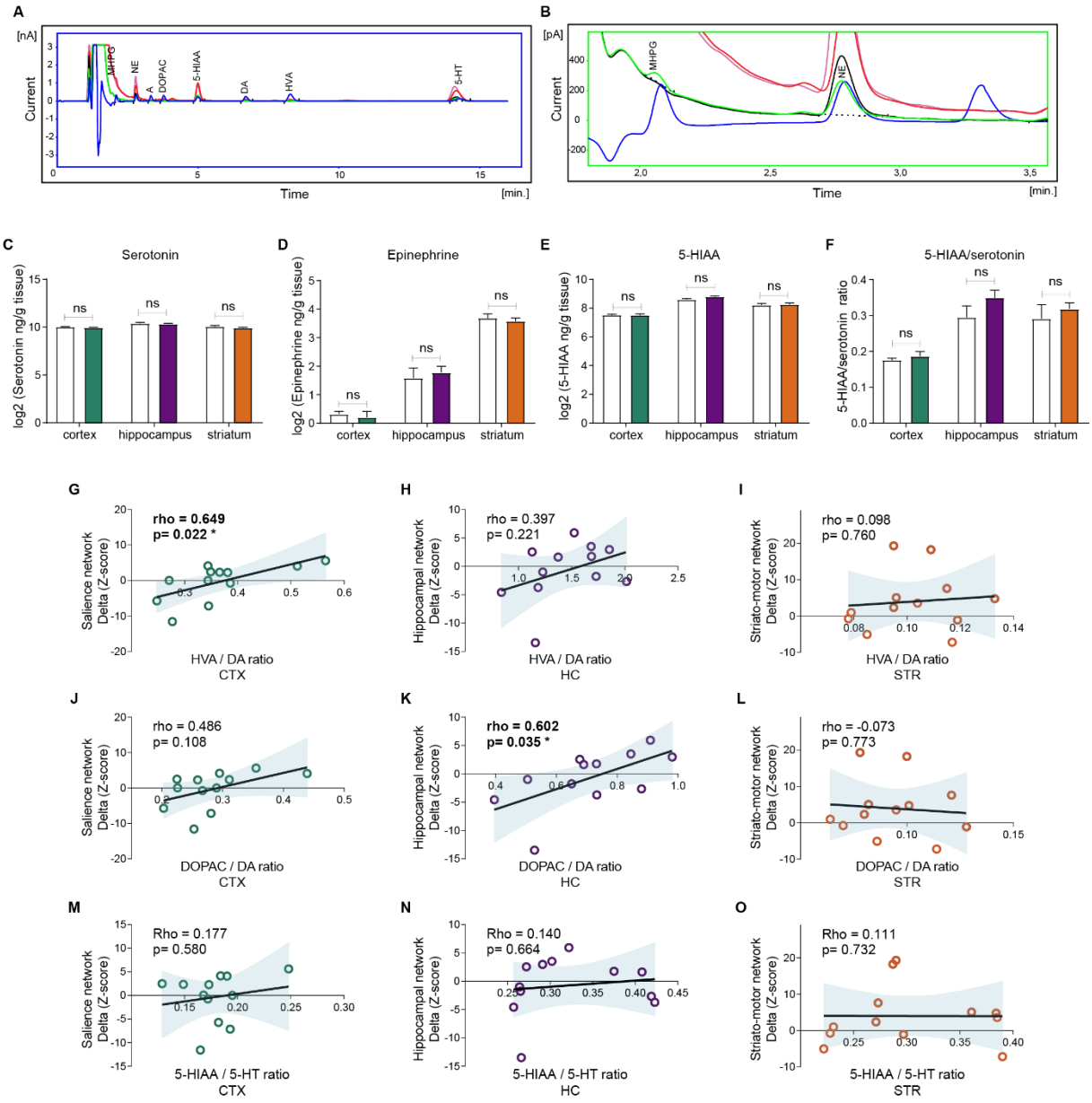

Figure S6. Related to Figure 6. (**A**) uHPLC chromatograms of hippocampus samples from an mCh mouse (undiluted in pink, 3 times diluted in black), an hM3Dq-mCh mouse (undiluted in red, 3 times diluted in green) and the standard (blue). (**B**) Magnification of (**A**) showing the chromatogram from an hM3Dq-mCh mouse with higher MHPG and lower NE values (green) resulting in a high norepinephrine turnover ratio (MHPG/NE), in contrast with the chromatogram from an mCh mouse (black). The standard is in blue. 5-HIAA: 5-hydroxyindoleacetic acid, 5-HT: 5-hydroxytryptamine (serotonin), E: epinephrine, DA: dopamine, DOPAC: 3,4-dihydroxyphenylacetic acid, HVA: homovanillic acid, MHPG: 3-methoxy-4-hydroxyphenylglycol, nA: nanoampere, NE: norepinephrine, pA: picoampere. (**C-F**) Levels of serotonin, epinephrine, 5-HIAA, and serotonin turnover (5-HIAA/serotonin ratio) remained unchanged in response to LC activation. Samples were collected 90 minutes after 0.03 mg/kg clozapine injection (two-way ANOVA), as explained in Figure 6A. Data represent mean ± SEM. (**G-O**) Spearman correlation coefficients Rho, and associated p-value (FDR corrected) between the turnover of DA (**G-L**) and 5-HT (**M-O**) in the cortex, hippocampus and striatum, and the changes in network connectivity in the Salience Network (left), Hippocampal Network (middle), and Striato-Motor Networks (right). (CTX: cortex, HC: hippocampus, STR: striatum = caudate putamen)

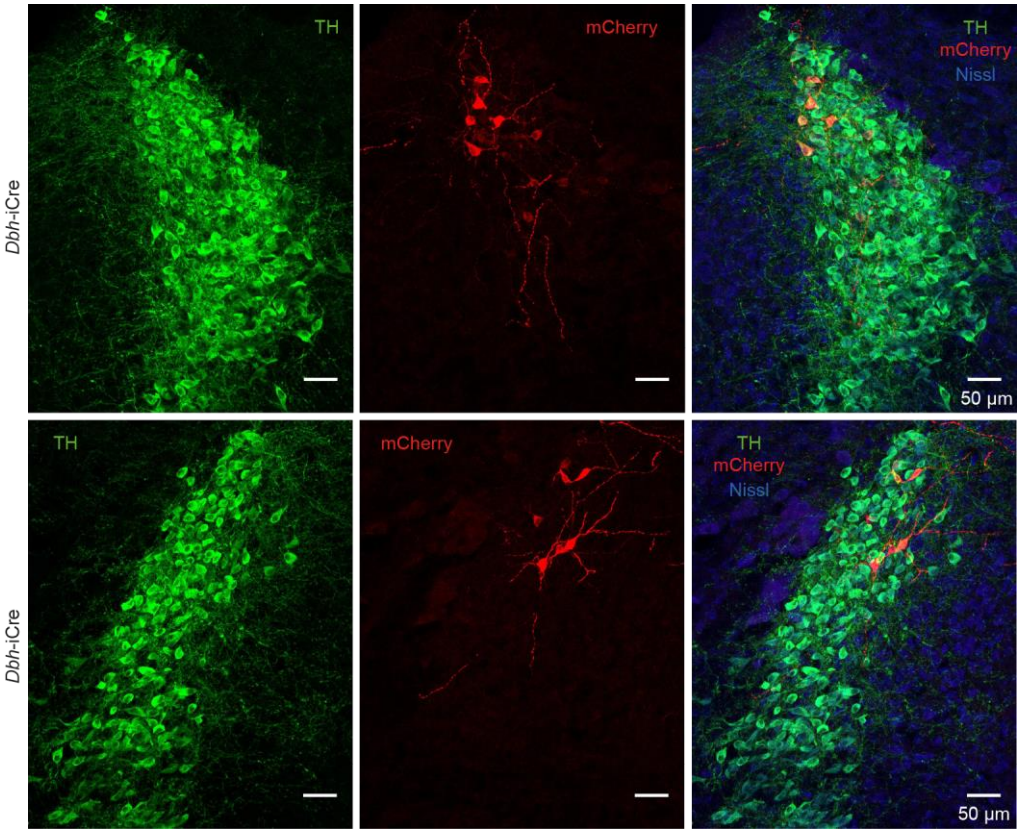

Figure S7. Related to Figure 7. Representative images from 2 DBH-iCre animals showing mCherry+ neurons in the LC after delivery of a Cre-dependent, mCherry-expressing retro-AAV2 in the dorsolateral caudate putamen.

Table S2. Related to Figure 4. Spearman's partial correlations considering multiple neuromodulatory receptor distributions. We calculated seven separate multiple regression models and determined Spearman's Rho (partial correlation) and associated P-value (FDR corrected) between the Node Modulation Index and the receptor distribution of interest after regressing out the contribution from all receptors belonging to a different neuromodulator family (i.e. adrenergic, dopaminergic, cholinergic nicotinic). Note that we did not partial out contributions from receptors within the same neuromodulator families due to their strong intrinsic co-expression. Significant correlations are indicated in bold.

Receptor distribution of interest	*Covariates of no interest*				
	Adrenergic	**Dopaminergic**	**Cholinergic**	**Spearman's Rho**	**p-value (FDR)**
Adrenergic Alpha-1		**x**	**x**	**0.2519**	**$4.11e^{-3}$**
Adrenergic Alpha-2		x	x	0.1269	0.1097
Adrenergic Beta-1		**x**	**x**	**0.2623**	**$7.75e^{-4}$**
Dopaminergic 1	**x**		**x**	**0.2005**	**0.0179**
Dopaminergic 4	**x**		**x**	**0.2219**	**0.0063**
Cholinergic Nicotinic Alpha-1	x	x		-0.011	0.8867
Cholinergic Nicotinic Gamma	x	x		0.030	0.7056